AGU ADVANCING EARTH AND SPACE SCIENCE

JGR Earth Surface

RESEARCH ARTICLE

10.1029/2020JF006027

Key Points:

- Linear inversion of longitudinal river profiles for the Central Anatolian Plateau southern margin uplift history
- Strong Quaternary uplift pulse that affected the margin of the plateau with evidence of eastward migration of the uplift through time
- Possible relation between uplift timing and rates with the break-off of the Cyprus slab

Supporting Information:

Supporting Information may be found in the online version of this article.

Correspondence to:

S. Racano,
simone.racano@uniroma3.it

Citation:

Racano, S., Schildgen, T. F., Cosentino, D., & Miller, S. R. (2021). Temporal and spatial variations in rock uplift from river-profile inversions at the Central Anatolian Plateau southern margin. *Journal of Geophysical Research: Earth Surface*, *126*, e2020JF006027. https://doi.org/10.1029/2020JF006027

Received 9 DEC 2020
Accepted 25 JUN 2021

Temporal and Spatial Variations in Rock Uplift From River-Profile Inversions at the Central Anatolian Plateau Southern Margin

Simone Racano[1,2], Taylor F. Schildgen[1,3], Domenico Cosentino[2], and Scott R. Miller[4]

[1]Helmholtz-Zentrum Potsdam, Deutsches GeoForschungsZentrum GFZ, Potsdam, Germany, [2]Department of Science, Roma Tre University, Rome, Italy, [3]Institute for Geosciences, University of Potsdam, Potsdam, Germany, [4]Department of Geology and Geophysics, University of Utah, Salt Lake City, UT, USA

Abstract In geodynamically active areas, spatio-temporal variations in rock uplift can provide key insights into the processes responsible for the evolution of topography. The Central Anatolian Plateau (CAP) southern margin experienced a rapid rock-uplift pulse with maximum rates of 3.5 m/kyr during the Quaternary, based on marine sediments dated to the middle Pleistocene that are now located at 1,500 m.a.s.l. Fluvial landscapes record elements that reflect temporal and spatial variations in rock-uplift rates, such as the normalized river steepness index, which is affected by rock-uplift rate, the erodibility of the underlying rock, and climate. Following the calibration of river profiles for an erosion coefficient value, which can be done using independent data (in our case, uplifted marine terraces and dated marine sediments), river profiles can be inverted for the rock-uplift histories that created them. Here, we demonstrate how it is possible to define the spatio-temporal rock-uplift history of the CAP southern margin by quantitative analysis of river profiles.

Plain Language Summary The cause of mountain building can be enigmatic, particularly in locations where evidence for typical causes, such as horizontal crustal shortening, is absent. However, forces in the lithosphere can come about in other ways that also cause the land surface to rise. The pattern and history of topographic growth, reconstructed from geologic evidence, is one way to test among different potential mechanisms. Here, we explore the rapid rise of the Central Anatolian Plateau in southern Turkey. We use the shape of the rivers that drain the plateau to reconstruct the history of topographic growth. These rivers set their gradients to balance rates of rock uplift, and thus they preserve evidence of past rates of rock uplift along their lengths, much like a tape recorder. We find that the most rapid phase of uplift began about half a million years ago and was short-lived everywhere, lasting only a few hundred thousand years, and occurred first in the west and later in the east. These results are similar to the effects predicted when one tectonic plate that is subducting beneath another breaks off, thus releasing a weight that allows the surface to rebound at rates that are among the fastest known on Earth.

1. Introduction

High-elevation, low relief plateaus, such as the Himalayan-Tibetan Plateau and the Altiplano-Puna Plateau, represent singular topographic features on the Earth surface that are often considered responsible for both local and global climate changes (Ehlers & Poulsen, 2009; Gregory-Wodzicki, 2000; Harris, 2006; Hartley, 2003; Lenters & Cook, 1997; Molnar et al., 1993; Ruddiman & Kutzbach, 1989; Strecker et al., 2007; Zhisheng et al., 2001). The Western Alpine-Himalayan orogenic belt, which resulted from the collision between Arabia with Eurasia starting at circa 20 Ma (Ballato et al., 2011; Okay et al., 2010) along the Bitlis-Zagros thrust zone, hosts the main orogenic plateau of the eastern Mediterranean region: the Central Anatolian Plateau (CAP) (Figure 1). The mechanisms that created the modern CAP topography remain debated, but have primarily been attributed to crustal and upper-mantle dynamics related to interactions among the Eurasian, African and Arabian plates (Bartol & Govers, 2014; Biryol et al., 2011; Cosentino et al., 2012; Faccenna et al., 2006; Fernández-Blanco et al., 2019, 2020; Göğüş et al, 2017; McPhee et al., 2018; Meijers et al, 2018; Öğretmen, Cipollari, et al., 2018; Racano et al., 2020; Schildgen, Cosentino, Bookhagen, et al., 2012; Schildgen, Cosentino, Caruso, et al., 2012; Schildgen et al., 2014). Considering that the plateau

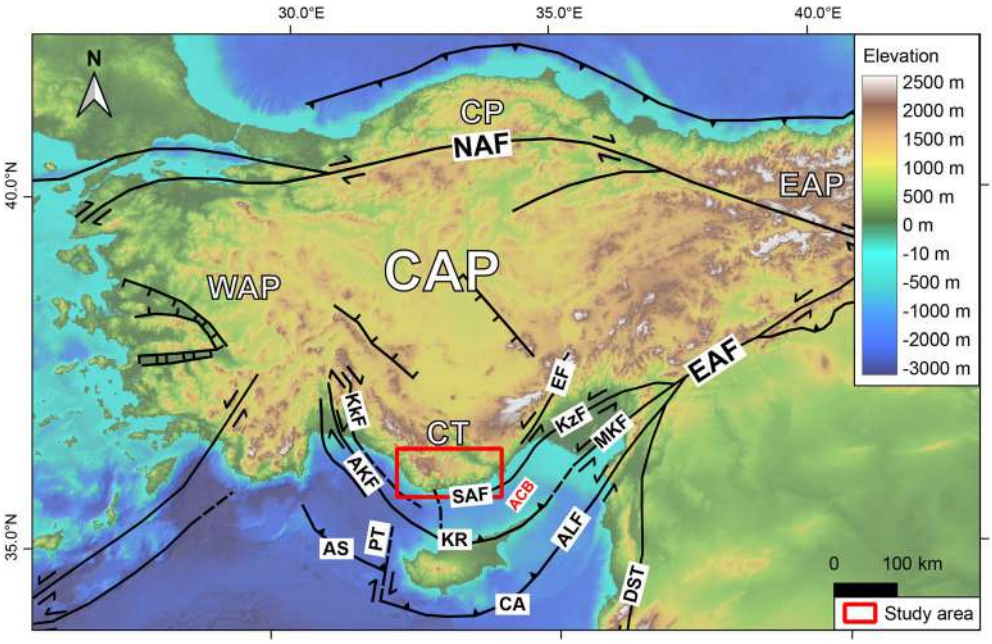

Figure 1. Regional simplified tectonic boundaries and topography of the Anatolian Microplate (modified from Cosentino et al., 2012 to Yildirim, Melnick, et al., 2013). CAP, Central Anatolian Plateau; EAP, Eastern Anatolian Plateau; WAP, Western Anatolian Province; NAF, North Anatolian Fault; EAF, East Anatolian Fault; DST, Death Sea Transform Fault; CA, Cyprus Arc; PT, Paphos Transform; AS, Antalya Slab; ALF, Amos-Larnaka Fault; KA, Kyrenia Range; AKF, Aksu-Kyrenia Fault; KkF, Kirkkavak Fault; SAF, Silifke-Anamur Fault; EF, Ecemiş Fault; KzF, Kozan Fault; MKF, Misis-Kyrenia Fault; ACB, Adana-Cilicia Basin. Red box shows region of Figure 2.

margins rise high above the plateau interior in Central Anatolia, different mechanisms are likely responsible for surface uplift of the plateau margins and the plateau interior (Göğüş et al., 2017).

Isotopic, geomorphic, and biostratigraphic observations constrain the topographic development of the CAP. In Central Anatolia, $\delta^{18}O$ analysis of Oligo-Miocene lacustrine carbonates suggests the absence of significant orographic barriers at both the northern and southern plateau margins prior to 20–16 Ma (Lüdecke et al., 2013). A steady decrease in $\delta^{18}O$ values between ca. 11 and 5 Ma was interpreted to indicate late Miocene surface uplift of the CAP southern margin (Meijers et al., 2018). Schildgen, Cosentino, Bookhagen, et al. (2012) used uplifted marine sediments and qualitative river-profile analysis to suggest two main rock-uplift phases at the southern margin: An initial slower phase starting after ca. 8 Ma, and a more rapid phase after ca. 1.6 Ma. Stratigraphic analysis has been used to refine the timing of these two main rock-uplift phases, the first at the end of the Miocene (5.45–5.33 Ma, Radeff et al, 2017), and the second during the middle Pleistocene (after 0.467 Ma, Öğretmen, Cipollari, et al., 2018). Modeling the evolution of interpreted marine terraces along the CAP southern margin indicates the middle Pleistocene rock-uplift pulse occurred during MIS7 (210–240 ka), with maximum uplift rates estimated at 3.4–3.8 m/kyr (Racano et al., 2020).

Despite these constraints on the rock-uplift history, uncertainties remain concerning the uplift mechanisms. Recent studies have related the topographic evolution of the southern CAP and the island of Cyprus to thermo-viscous forearc uplift associated with subduction, whereby compression led to the mechanical, brittle, upper-crustal strain that created the Cyprus forearc system, and also the thermal, ductile, lower-crustal deformation that propelled CAP growth (Fernández-Blanco et al., 2019, 2020). These studies predict the gradual growth of regional topography to kilometer-scale heights in the Central Taurides before the Pliocene (Fernández-Blanco et al., 2019, 2020; Meijers et al., 2018). Alternative proposed mechanisms for uplift of the CAP southern margin include continental collision (McPhee & van Hinsbergen, 2019), or break-off of the Cyprus slab (Cosentino et al., 2012; Radeff et al., 2016, 2017; Schildgen, Cosentino, Bookhagen, et al., 2012; Schildgen, Cosentino, Caruso, et al., 2012) with a majority of the modern topography having been created since the middle Pleistocene (Öğretmen, Cipollari, et al., 2018; Racano et al., 2020). The latter mechanism could result in a pulse of brief but extremely fast rock uplift (i.e., several km/Myr for less than

1 Myr) if the break-off event is relatively shallow (Duretz & Gerya, 2013). Furthermore, if a slab break-off event occurs through lateral progression of a slab tear, the rock-uplift history could show a spatio-temporal pattern that mimics the propagation direction of the tear (i.e., parallel to the strike of the subduction zone) (Wortel & Spakman, 2000). This spatio-temporal pattern of rock uplift would contrast with the rock uplift associated with crustal thickening linked to subduction-induced strain or continental collision, which would be slower, prolonged, and potentially continuous along strike.

Because tectonics and topography are strongly linked in regions that have experienced recent deformation (e.g., Wobus et al., 2006), the topographic evolution of the CAP southern margin can be used to evaluate the predictions of the various geodynamical models. Such a record is commonly expressed in longitudinal profiles of rivers, which can be used to quantitatively assess spatial and temporal patterns of rock uplift (Kirby & Whipple, 2012). A growing endeavor in tectonic geomorphology is to infer the rock-uplift (or base-level fall) history by inverting river profiles. Because the position of a point along a river profile is defined by the balance between rock uplift and erosion, and perturbations to the rock-uplift rate tend to propagate upstream along the profile (e.g., Howard & Kerby, 1983; Tucker & Slingerland, 1996; Whipple et al., 1999), along-channel variations in elevation can be inverted for a rock-uplift history if certain testable assumptions about the mechanisms of fluvial erosion are met (Fox et al., 2014, 2015; Gallen, 2018; Goren et al., 2014; Li et al., 2020; Ma et al., 2020; McNab et al., 2018; Pritchard et al., 2009; Roberts, Paul et al, 2012; Roberts & White, 2010; Roberts, White, et al., 2012).

In this paper, we present an overview of the morphostructural and fluvial features of the CAP southern margin. In particular, we highlight patterns in river steepness and potential drainage divide disequilibrium in response to rock uplift. Next, we present a detailed, spatially focused, and locally calibrated linear inversion of river profiles. Whereas previous work has used similar river-profile inversions to assess the spatio-temporal history of rock uplift over the whole of Anatolia, those results differ fundamentally from ours because of a different calibration (McNab et al., 2018). We demonstrate that the basic assumptions of linear inversion are met in our study region and that the results are consistent with records of rock uplift preserved in a flight of coastal planation surfaces interpreted to be Quaternary marine terraces. Additionally, we show how the rock-uplift history of the CAP southern margin varies spatially, and we discuss how these inferred patterns are robust despite uncertainties in the models. Finally, we use our results to assess which geodynamic mechanism best explains the inferred rates and spatial patterns of rock uplift.

2. Regional Tectonic Setting and Uplift History

The tectonic setting of central Anatolia is a consequence of the convergence of the African and Arabian plates relative to the Anatolian plate (Reilinger et al., 1997). The stresses between these plates are partly compensated by the westward movement of the Anatolian plate along North Anatolian and East Anatolian Fault Zones (Barka & Kadinsky-Cade, 1988; Burke & Şengör, 1986; Dewey & Şengör, 1979; Ketin, 1948; McKenzie, 1978; Şengör, 1980; Şengör et al., 1985). Several intraplate tectonic elements delimit the CAP (Figure 1), separating it from the contractional Eastern Anatolian Plateau and the predominantly extensional Western Anatolian Province (Büyüksaraç et al., 2005). At the eastern CAP limit, the transtensional Ecemiş and Kozan faults continue offshore to become the transtensional Silifke-Anamur Fault Zone. The western CAP limit is also defined by two major transtensional faults, the Kirkkavak and the Aksu-Kyrenia faults (Aksu et al., 2005, 2014; Güneş et al., 2018) (Figure 1).

2.1. Uplift Constraints of the CAP Margins

The northern and southern margins of the CAP show substantial differences in their Quaternary rock-uplift histories. Rock uplift at the northern margin of the CAP has been explained by crustal thickening along a restraining bend in the North Anatolian fault zone, resulting in rock-uplift rates of 0.2–0.3 m/kyr since ca. 400 ka within the Central Pontides based on marine and river terraces (Yildirim, Melnick, et al., 2013; Yildirim, Schildgen, et al., 2013). Terraces near the Kızılırmak River outlet yielded similar rock-uplift rates of 0.28 ± 0.07 m/kyr since 545 ka (Berndt et al., 2018). Within the east-central part of the plateau interior, Çiner et al. (2015) used fluvial terraces of the northward draining Kızılırmak River to estimate a mean incision (and inferred rock-uplift) rate of 0.051 m/kyr for the last 1.9 Ma. In south-central Anatolia, Aydar

et al (2013) used the incision of well-dated volcanic sequences to determine that incision started after 5 Ma, with rates of 0.12 m/kyr from 5 to 2.5 Ma and 0.04 m/kyr since 2.5 Ma.

In contrast, the southern CAP margin appears to show a faster and more complex rock-uplift history divided into two main stages. Stratigraphic analysis in the Adana-Cilicia basin, which lies southeast of the CAP southern margin, indicates the deposition of ∼1.7 km of clastic sediments derived from the Central Taurides, corresponding to the first rock-uplift phase at the end of the Messinian, ca. 5.45 to 5.33 Ma (Radeff et al., 2016, 2017; Öğretmen, Cipollari, et al., 2018). The second, faster rock-uplift phase has been constrained by biostratigraphic and morphostratigraphic analyses. Qualitative analysis of river profiles, dated river terraces, and the position of early Pleistocene marine sediments initially pointed to faster rock uplift since the early Pleistocene (Schildgen, Cosentino, Bookhagen, et al., 2012). This rapid rock-uplift phase was more precisely constrained following the discovery of early Pleistocene (Calabrian) to middle Pleistocene marine sediments capping the margin together with a paleoshoreline at a maximum elevation of 1,400–1,500 m.a.s.l. dated to 0.467 Ma based on analyses of benthic and planktonic foraminifers, ostracods, and calcareous nannofossils (Öğretmen, Cipollari, et al., 2018). The rock-uplift history since that time is inferred from modeling of a staircase sequence of coastal planation surfaces from the top of the margin toward the sea that have been interpreted as marine terraces (Racano et al., 2020). These terrestrial deposits and landforms indicate that a pulse of fast rock uplift occurred during the middle Pleistocene (MIS7), with maximum rock-uplift rates estimated to have been 3.4–3.8 m/kyr (Racano et al., 2020).

2.2. Subducting Slab Geometry

Tomography has revealed a complex picture of the subducting African plate under the Anatolian plate today, with multiple slab windows separating the plate into distinct slabs: The Aegean slab beneath western Turkey, the Cyprus slab beneath Central Anatolia (sometimes separated into western and eastern Cyrus slabs), and the Bitlis slab beneath eastern Turkey (Biryol et al., 2011; Menant et al., 2016; Portner et al., 2018; Kounoudis et al., 2020). Whereas break-off of the Bitlis slab is well established based on a deep, fast anomaly that is unconnected to the subduction zone, a possible break in the Cyprus slab is barely resolvable, implying that it has either not happened or is very recent. Break-off of the Bitlis slab has been estimated to have occurred during the middle to late Miocene based on the timing of magmatic events (Çolakoğlu & Arehart, 2010; Ekici, 2016; Keskin, 2003, 2007; Keskin et al., 1998; Şengör et al., 2008). An inferred break-off of the Cyprus slab has been suggested sometime from late Miocene to middle Pleistocene based on thermochronology (Karaoğlan, 2016; Karaoğlan et al., 2016), crustal deformation (Kaymakci et al., 2010), stratigraphy (Cosentino et al., 2012; Öğretmen, Cipollari, et al., 2018; Öğretmen, Frezza, et al., 2018; Radeff et al., 2017), and paleotopographic analysis (Schildgen et al., 2014).

3. Materials and Methods

Strong variations in Quaternary rock-uplift rates should leave a clear signal in the landscape morphology. In drainage systems of the southern CAP margin, where variations in climate and rock erodibility are relatively small, major knickpoints along river long profiles and significant changes in river gradient likely reflect variations in rock-uplift rates through time. In our analyses, we focused on rivers that drain from the top of the CAP southern margin directly toward the Mediterranean Sea. We analyzed 1-arc s (∼30 m resolution) Shuttle Radar Topography Mission digital topography (downloaded from https://earthexplorer.usgs.gov/) using TopoToolbox (Schwanghart & Scherler, 2014), a MATLAB® toolbox for geomorphological analysis, together with topographic analysis tools from the TAK toolbox (Forte & Whipple, 2019).

3.1. Topographic Metrics

We analyzed a slope map derived from the DEM to define the limit of the plateau margin and study variations along its seaward flanks. We also calculated local relief (Stearns, 1967) with a circular sampling window of 2 km radius, which illustrates the characteristic valley-to-ridge relief pattern. We used topographic metrics and the channel steepness index (see next paragraph) to assess the equilibrium conditions between catchment divides (e.g., Whipple et al., 2017; Scherler & Schwanghart, 2020).

3.2. River Profiles

The evolution of a river profile can be described as the change in elevation of a point on a channel through time, which relates to the competition between erosion (E) and rock uplift (U):

$$\frac{dz(t,x)}{dt} = U(t,x) - E(t,x), \tag{1}$$

Graded river profiles are commonly characterized by an empirical power-law relationship between the local channel slope (S) and the upstream drainage area (A):

$$S = k_s A^{-\theta}, \tag{2}$$

where k_s is the channel steepness index and θ is the concavity index (Hack, 1957, 1960; Flint, 1974). The steepness index is highly variable but the concavity index typically has values ranging between 0.3 and 0.6 in steady-state channel profiles (Kirby & Whipple, 2012; Tucker & Whipple, 2002).

The erosion rate of a bedrock river channel can be described by the stream power equation:

$$E = KA^m \left(\frac{dz}{dx}\right)^n, \tag{3}$$

where dz/dx is the local channel gradient, K is the erosion coefficient, which is related to lithology and climate, and m and n are two positive coefficients related respectively to basin hydrology and erosion processes in the channel (Howard, 1994; Whipple & Tucker, 1999).

Equation 3 can be rearranged such that:

$$\frac{dz}{dx} = \left(\frac{E}{K}\right)^{1/n} A^{-(m/n)}. \tag{4}$$

By comparison with Equation 2, the empirical exponent θ is seen to be equal to the ratio between m and n. If the river profile is in steady-state, the channel erosion rate (E) will be equal to the rock-uplift rate (U),

$$\left(\frac{U}{K}\right)^{1/n} = \left(\frac{dz}{dx}\right) A^{m/n}. \tag{5}$$

From Equation 5, we obtain a new equation that describes how the steepness index (k_s) relates to E, U, and K:

$$\left(\frac{E}{K}\right)^{1/n} = \left(\frac{U}{K}\right)^{1/n} = \left(\frac{dz}{dx}\right) A^{m/n} = k_s. \tag{6}$$

Harkins et al. (2007) and Perron & Royden (2013) developed a procedure to transform river longitudinal profiles such that steady-state forms will plot as a straight line, with a slope equal to the ratio of rock-uplift rate over erodibility. To do so, we solve for dz/dx in Equation 4, and then integrate considering U (instead of E) and K are spatially variable:

$$\int dz = \int \left(\frac{U(x)}{K(x)A(x)^m}\right)^{1/n} dx. \tag{7}$$

Performing the integration in the upstream direction from a base level x_b to an observation point x yields the equation:

$$z(x) = z(x_b) + \int_{x_b}^{x} \left(\frac{U(x)}{K(x)A(x)^m}\right)^{1/n} dx. \tag{8}$$

In the case where U and K are spatially constant, Equation 8 can be reduced to the form:

$$z(x) = z(x_b) + \left(\frac{U}{K}\right)^{1/n} \int_{x_b}^{x} \frac{dx}{A(x)^{m/n}}. \tag{9}$$

Introducing a reference drainage area (A_0), river profiles can be transformed river with units of length on both axes, such that the coefficient and integrand in the trailing term are dimensionless:

$$z(x) = z(x_b) + \left(\frac{U}{KA_0^m}\right)^{1/n} \chi, \tag{10}$$

where χ is an integration of river horizontal coordinates defined by the equation:

$$\chi = \int_{x^b}^{x} \left(\frac{A_0}{A(x')}\right)^{m/n} dx'. \tag{11}$$

The new representation of the long-river profile, elevation versus χ, known as the χ plot, is a straight, positively sloping line for concave-upward river channels. The slope of the χ plot is proportional to the steepness index, k_s. Excluding influences on the channel slope associated with lithological contrasts and anthropogenic elements (e.g., dams), higher rock-uplift rates are associated with steeper slopes on the χ plot (i.e., greater k_s). The plot will therefore show breaks-in-slope if knickpoints are present (i.e., separating areas of higher and lower steepness).

We obtained the normalized steepness index values (k_{sn}) for all channels by calculating channel steepness based on a selected reference concavity index (θ_{ref}). The normalized steepness index is a robust measure of relative channel steepness throughout a region and is not sensitive to the exact choice of θ_{ref} (Wobus et al., 2006). We determined the most representative θ of all the catchments draining the plateau margin to the sea by the χ-z plot minimization method (Goren et al., 2014) to calculate k_{sn}, for all channels above a minimum drainage area of 1 km^2. Channels were extracted after we reduced the noise on the DEM elevations by applying a moving average window of 500 m along channels. We analyzed k_{sn} and χ values of the main river trunk streams in eight selected basins to obtain qualitative overviews of rock-uplift histories (based on plots of k_{sn} vs. elevation). Although there are variations in rock type throughout the study region, with a greater prevalence of metamorphic rocks in the west and sedimentary rocks in the east (as will be discussed in greater detail later), along individual trunk streams, the variations in rock type (and inferred erodibility) are small. Nevertheless, we marked along the profiles only the knickpoints that are clearly unrelated to changes in lithology. k_{sn} and χ indexes were calculated for three different θ (or m/n) values (0.3, 0.4, and 0.5).

3.3. Rock-Uplift Histories From Linear Inversions of River Profiles

Following Goren et al. (2014), the response time τ represents the travel time of a perturbation along the river profile from the river outlet ($x = 0$) to a given point x, and can be expressed by the equation:

$$\tau = \int_{0}^{x} \frac{dx'}{K(x')A(x')^m S(x')^{n-1}}. \tag{12}$$

Comparing Equations 11 and 12, one notes that τ maps linearly with χ when $n = 1$ and K is constant, but importantly, τ can account for spatial variations in the erodibility of different rocks because the equation includes path-dependent changes in the erosion coefficient K. When $n = 1$, perturbations that reflect the base-level-fall history of the river migrate upstream at a rate that is solely a function of K and the upstream drainage area. Put another way, the perturbation migration rate is not a function of slope, and thus the time-record of base level fall is not artificially created or destroyed at changes in slope such as knickpoints. This assumption allows τ to be the basis for the linear inversion of river profiles to study the rock-uplift/base-level fall history recorded in fluvial topography (Gallen, 2018; Pritchard et al., 2009; Roberts & White, 2010).

Several studies have employed a spatially uniform erosion coefficient to solve the inverse problem, solving for rock uplift as a function of space and time on continental scales (McNab et al., 2018; Pritchard et al., 2009; Roberts & White, 2010). Although it may be difficult to justify the assumption of uniform K over such a large region, this assumption may be safer in smaller areas with rock types of similar erodibility and relatively uniform climate.

Assuming $n = 1$, Equation 12 becomes:

$$\tau = \int_0^x \frac{dx'}{K(x')A(x')^m}. \tag{13}$$

For a block-uplift scenario, the elevation of the river network can be predicted by the equation:

$$z(x) = \int_{-\tau(x)}^{0} U(t')dt'. \tag{14}$$

where t' is the integration variable, time zero is the present, and the past is represented by negative time. Equation 14 predicts that the present elevation of a given point along a river network $z(x)$ is the integral of the relative rock-uplift rate along the downstream channel points during the past over a duration of $\tau(x)$ and that all tributaries with the same $\tau(x)$ will lie at the same elevation $z(x)$.

Following Gallen (2018) and Goren et al. (2014), we reconstructed the rock-uplift history from the river network during discrete time intervals using Equation 14, supposing a spatially and temporally constant K. The data organization assumes that N data points of z and τ along the fluvial network that are ordered according to elevation because they share a common rock-uplift history (Gallen, 2018).

By this discretization, Equation 14 can be written for each data point and the equations can be organized in matrix form:

$$\mathbf{AU} = \mathbf{z}, \tag{15}$$

where $\mathbf{A}$ is an $N\,x\,q$ matrix, q is the number of time intervals, $\mathbf{U}$ is the rock-uplift (or baselevel-fall) rate and $\mathbf{z}$ is the elevation. This is an overdetermined inverse problem, as there are more known data points than unknown parameters. As such, a least squares estimate for $\mathbf{U}$ is used (Tarantola, 1988):

$$\mathbf{U} = \mathbf{U_{pri}} + \left(\mathbf{A}^T\mathbf{A} + \Gamma^2\mathbf{I}\right)^{-1}\mathbf{A}^T\left(\mathbf{z} - \mathbf{AU_{pri}}\right), \tag{16}$$

where Γ is a dampening coefficient that determines the smoothness imposed on the solution $\mathbf{I}$ is the $q \times q$ identity matrix and $\mathbf{U_{pri}}$ represents the prior guess at the rock-uplift rate. Gallen (2018) estimated $\mathbf{U_{pri}}$ with the equation:

$$\mathbf{U_{pri}} = \left(\frac{1}{N}\right)\sum_{i=1}^{N}\left(\frac{z_i}{\sum_{j=1}^{q}\mathbf{A}_{i,j}}\right). \tag{17}$$

In our river-profile inversions, an optimal Γ is automatically calculated by the normalized misfit between the elevation of the river pixels and the predicted elevations with the inferred rock-uplift history (following Goren et al., 2014), and is optimized for each basin and imposed K value.

A constant time step ΔT of 50 kyr was chosen to determine the number of discrete time intervals in the inversion, as this time step produced lowest misfits between the observed and empirical τ plots (Figure S1). The other assumption implicit in the results of the inversion is that basin divides in the area where the river inversion is performed are stable over the duration of the inversion. We test this assumption (see Supporting Information) and find that it is reasonable for this application. Finally, we performed river-profile inversions for discrete river basins in the study area, using stream channels that drain from the top of the margin toward the sea.

We estimated the erosion coefficient K by rearranging Equation 6 and determining the ratio between rock-uplift rate and the normalized steepness index from Equation 6

$$K = \frac{U}{\left(k_{sn}\right)^n}. \tag{18}$$

For this estimate, we utilize the rock-uplift rates inferred from modeling of interpreted marine terraces on the eastern side of the CAP southern margin by Racano et al. (2020). In that study, the creation and uplift of marine terraces were modeled with a landscape evolution model together with their inferred ages and an assumed sea-level history to derive a rock-uplift history. Each marine terrace represents an amount of rock uplift since a specific point in time, and the interval between two adjacent terraces represents a time-averaged rate of rock uplift between two points in time. Importantly, the stream power equation predicts that if $n = 1$, vertical movement of knickpoints (or any steepened sections of the channel) will track rock-uplift rates, and hence they will also track with vertical movement of the marine terraces (Niemann et al., 2001; Perron & Royden, 2013). Thus if we assume $n = 1$, we can compare rock uplift rates from given time intervals in the past with the steepnesses of spatially corresponding stream channels. Moreover, the plotted relationship between rock uplift rates and channel steepness provides a check on the value of the slope exponent n: If the relationship is linear, then n is consistent with a value of one, which is a crucial assumption for the linear inverse model. Such a relationship is unlikely to be biased by the assumption required for our elevation-based binning technique that n is 1.

To estimate K using the approach above, we divided the eastern catchments (basins 5–8), where marine terraces are developed (Racano et al., 2020), into elevation bands based on the elevation ranges of the marine terraces and extracted the k_{sn} values at every channel cell in each band. Next, we estimated the slope of the linear relationship between the average rock-uplift rate and the average k_{sn} for each elevation band using a York regression (York et al, 2004) forced through the axis origin, and equated this slope to K (Equation 18). The x and y errors used for the data points in the regression are one standard deviation of the mean of both k_{sn} in each elevation band and the rock-uplift derived from marine terrace modeling (Racano et al., 2020). This approach enabled us to take into account x and y errors and respect the linearity in Equation 6 that is used to infer K.

We verified the goodness of our estimation by determining K a second way, performing a sequence of river inversions arbitrarily varying K and searching for the erosion parameter that generates the lowest misfit between the cumulative rock uplift estimates from the river profile inversion and from interpreted marine terraces (Racano et al., 2020) (Supporting Information). While this method does not directly test whether n is 1, it has the advantage of being insensitive to errors in channel steepness that can arise based on DEM resolution and profile smoothing.

To explore the impacts of the assumptions we make when performing river-profile inversions to derive rock-uplift histories, we performed sensitivity tests to evaluate the effect of selecting different numbers of rivers within each basin to include in the inversion, the impact of drainage migration or capture events, and the effect of different $\mathbf{U_{pri}}$ estimates. We include those results in the Supplementary material.

4. Results

4.1. Regional Topographic and Drainage-System Analysis

The CAP southern margin is topped by a high elevation, relatively low-relief surface that slopes gently eastward (Figures 2a, 2b and 2f). The maximum elevation of 2,250 m a.s.l. occurs north of Anamur; going toward the east, elevations decrease to 900 m west of Silifke, over a distance of 120 km (Figure 2f). A major knickzone of the drainage system defines the southern limit of the upper surface (Figure 2a; Schildgen, Cosentino, Bookhagen, et al., 2012).

West of this low-relief surface capping the CAP southern margin, elevations decrease rapidly to the west over a distance of 40 km until reaching sea level (Figure 2f). Overall, the southern flank of the margin is characterized by steep slopes that decrease toward the east (Figure 2b). West of Aydıncık, high slope values define the limit of the paleosurface atop of the margin. Between Aydıncık and Silifke, the limit is less evident due to the presence of staircase sequences of surfaces that have been recognized as marine terraces (Racano et al., 2020). The west-to-east decrease in slope is mimicked by the local relief (Figure 2c); toward

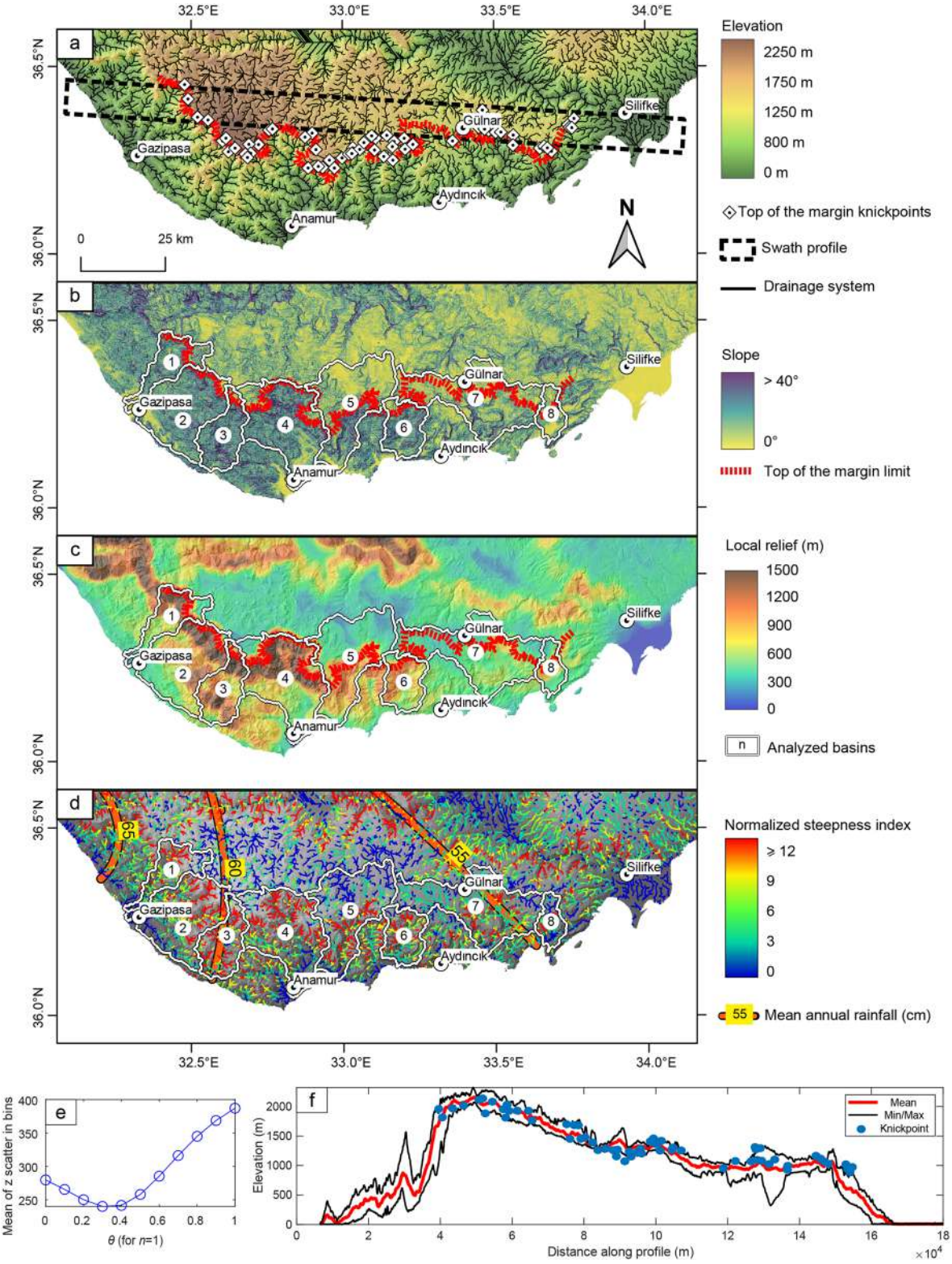

Figure 2. Topographic metrics at the southern margin of the Central Anatolian Plateau. (a) Topographic map, drainage basins analyzed for river-profile inversions, major knickpoints and trace of the swath profile (shown in f); (b) Slope map with margin of the plateau limit marked; (c) Local-relief map calculated with a circular sampling window of 2,000 m of radius, and analyzed basins; (d) k_{sn} map, with values calculated with a reference concavity value of 0.3 and contours of mean annual rainfall; (e) Estimation of the best concavity index for the rivers draining southern margin of the CAP; (f) Swath profile and main knickpoint elevations.

the west, maximum relief is between 1,200 and 1,500 m just below the low-relief upper surface, whereas toward the east, it is ca. 600 m. High maximum relief values also characterize the northern edges of the low-relief surface (Figure 2c).

The topographic differences in slope along the west-east axis of the southern CAP margin are also recorded in river steepness index values (k_{sn}). The k_{sn} map of the southern flank (Figure 2d) has been calculated with a reference concavity index of 0.3, which is the most representative θ value for the rivers draining the southern slope of the plateau (Figure 2e). Like the slope map, the k_{sn} map shows a decrease in values toward the east. Spatial variability in k_{sn} values can result not only from spatial and temporal variations in rock-uplift rate, but also from variations in lithology and climate. Mean annual precipitation varies somewhat across the margin: from ca. 60–70 cm in the west to ca. 50 cm in the east (Figure 2d). Based on empirical observations of the relationship between precipitation and k_{sn} (D'Arcy & Whittaker, 2014), which suggests that k_{sn} scales inversely with the square root of precipitation, the observed difference in rainfall is expected to have a minor (up to 17%) influence on k_{sn} values.

The geology differs more substantially; from basin 1 to basin 4 (Figure 3a), the bedrock is characterized by Paleozoic and Mesozoic metamorphic rocks (mostly represented by marbles and secondary outcrops of metapelites as schists and phyllites) and sedimentary rocks (mostly neritic limestones and clastic units such as sandstones, shales, and radiolarites). East of basin 5, there is a predominance of sedimentary rocks, such as neritic limestones and siliciclastic rocks, whereas the Tauride metamorphic bedrock comprises Mesozoic marbles. Shallow-water limestones, calcarenites, marls, and conglomerates represent the Miocene and Quaternary marine units that cover the deformed bedrock (Figure 3a). Despite this lithologic variability, not all river profiles show significant knickpoints where lithology changes (Figures 3b–3i), but they are marked by a major knickpoint at the edge of the margin-capping paleosurface (Figures 2a–2c). In all the profiles, the shape is broadly similar, showing low gradients in the uppermost portions of the drainage, then a dramatic increase in gradient farther downstream, then a decrease again at low elevation. The only profile that differs from the others is in Basin 7 (Figure 3f), which is probably related to the preservation of extensive marine terraces between 1,200 and 700 m. a.s.l (Racano et al., 2020). The k_{sn} values downstream from the major knickpoint are highest in the western drainage basins (1–4) and decrease toward the east (Figure 2d). Moreover, the elevations of the major knickpoints follow the same eastward decreasing trend as the elevation of the low-relief paleosurface (Figure 2e).

To better define the geomorphic signatures of rivers related to the rock-uplift history, we focused our analysis on the eight catchments that drain from the top of the margin toward the sea. We considered the main channels for each catchment that flow mostly perpendicular to the coast.

For rivers 1–4 (Figure 4), the elevations of the knickpoints that delimit the edge of the upper low-relief surface vary from 2,200 to 1,800 m.a.s.l. River 3 shows another knickpoint located around 400 m a.s.l. at a lithological change from Paleozoic metamorphic to Paleozoic/Mesozoic marine rocks. For rivers 5–8, the elevations of the major knickpoints decrease from 1,400 to 900 m.a.s.l. A well-defined knickpoint around 400–450 m.a.s.l. is also present in most of the analyzed rivers (except for rivers 1, 4, and 6), and is probably related to the development of marine terraces during the Quaternary (Racano et al., 2020).

In several of the χ plots, the major knickpoints identified along the upper portions of the river profiles can be seen as a prominent break in slope (Figure 4). In rivers 2, 3, 5, and 7, the signal is less evident, because of the short distance over which rivers cross the upper low-relief surface. The strong increases in k_{sn} suggested by the breaks in slope in the χ plots do not appear to be controlled by changes in lithology alone; river segments downstream from the knickpoints run on different rocks types that do not produce significant changes in the slopes of the plots. For rivers 1–5, the χ plots show their steepest slopes between the major knickpoints (at 1,800–2,200 m a.s.l.) and ca. 450–500 m a.s.l. The slopes of the χ plots rapidly decrease below 450–500 m a.s.l. For rivers 6–8, the highest slopes on the χ plots occur between the major knickpoints (at 1,400 to 900 m a.s.l.) and 150–300 m a.s.l. Again, the slopes of the χ plots decrease suddenly at lower elevations.

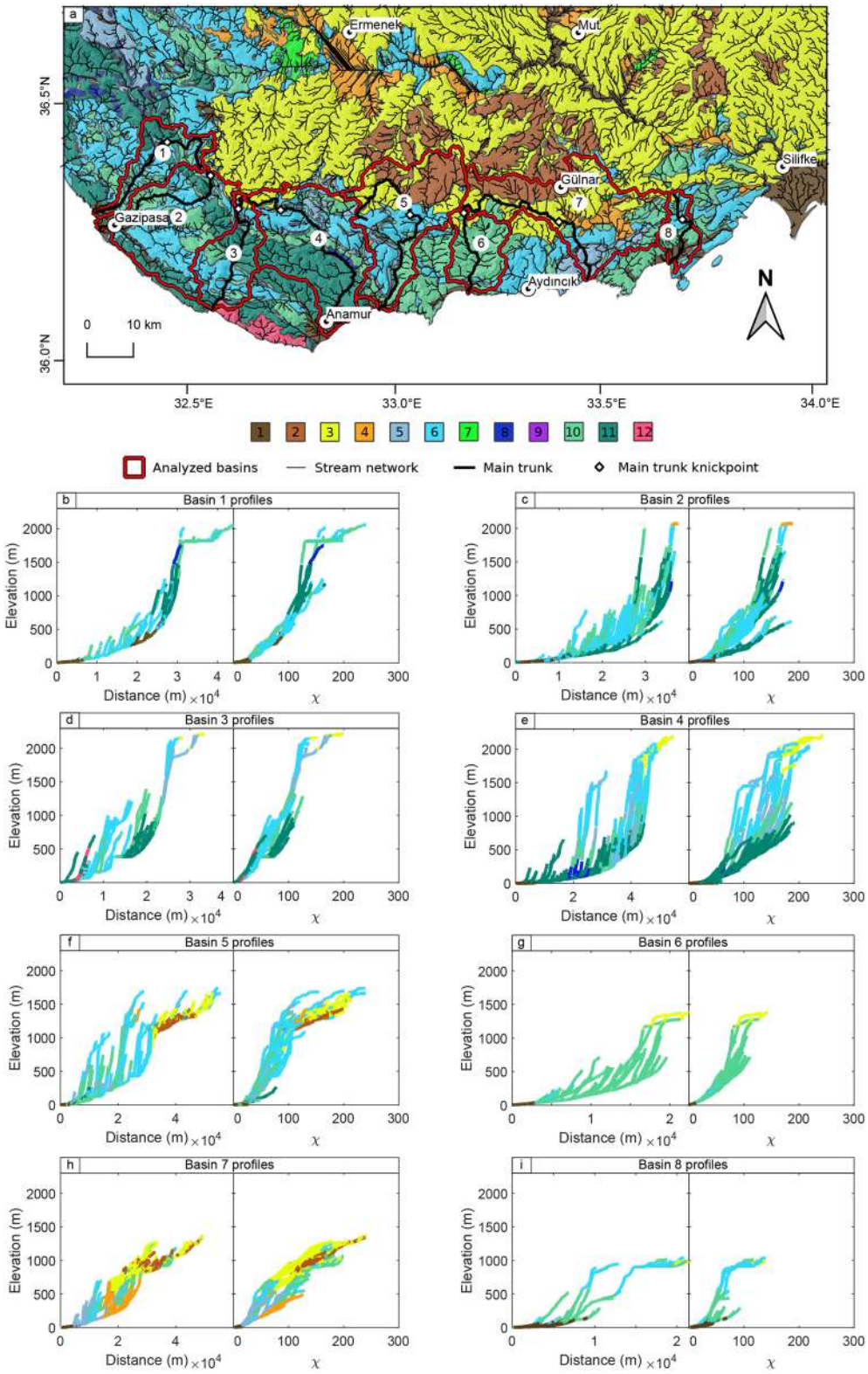

Figure 3. Geology and analyzed river basins. (a) Geological map of the Central Anatolian Plateau southern margin. Geology simplified from 1:500,000 scale geologic maps (Senel, 2002; Ulu, 2002): 1) Quaternary continental deposits; 2) Quaternary marine units (marls and calcarenites); 3) Miocene marine units (mostly neritic and shallow water limestones passing to marls in the area of Silifke); 4) Miocene clastic units (mostly conlomerates and breccias); 5) Mesozoic continental units (clastic rocks); 6) Mesozoic marine units (neritic limestones); 7) Mesozoic ophiolitic melange; 8) Mesozoic metamorphic units (marble and secondary metaflysch); 9)Triassic volcanic rocks (basalts); 10) Paleozoic marine units (carbonates and flysch); 11) Paleozoic metamorphic units (mainly foliated rocks and marbles); 12) Undifferentiated pre-Cambrian metasedimentary rocks; (b)–(i) river profiles of the analyzed basins colored by the geology.

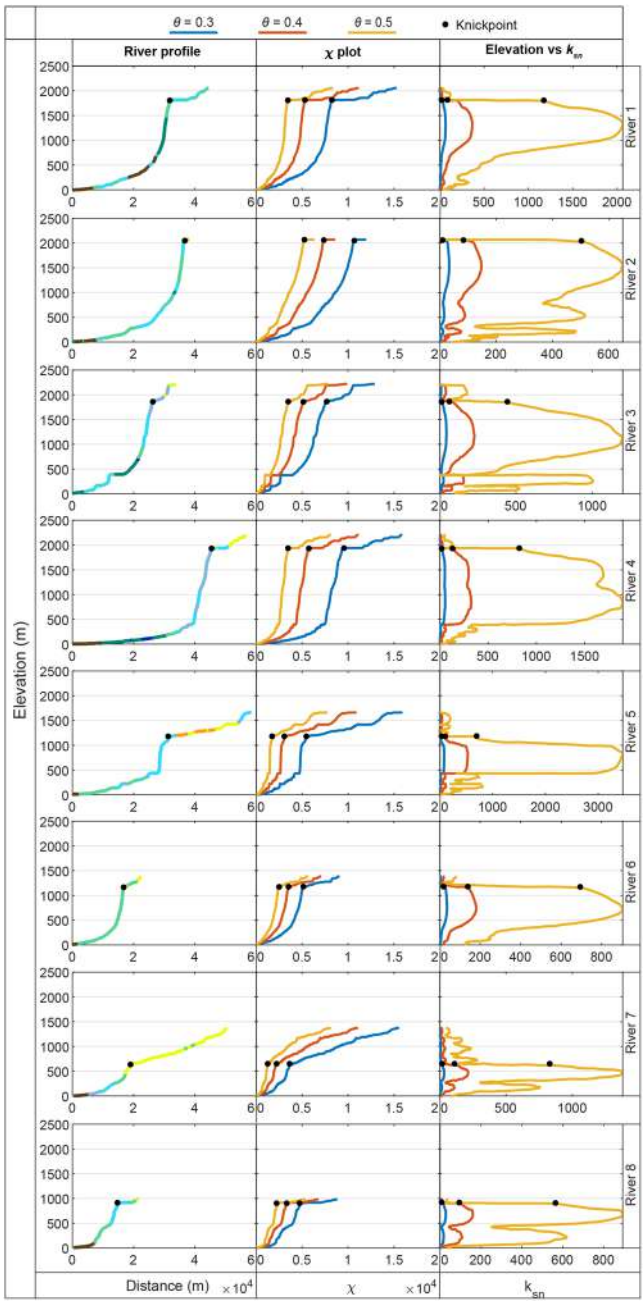

Figure 4. Qualitative analysis of the main trunks of the selected basins, illustrating river long profiles colored by lithology (legend in Figure 3), χ plots, and k_{sn} versus elevation plots for different θ values.

As noted earlier, the changes in slope of the χ-plots correspond to changes in k_{sn} values; this pattern persists regardless of the choice of θ (Figure 4). For each θ value, k_{sn} values increase starting from the major knickpoint on each profile, then reach peak values farther downstream. The elevations at which the highest k_{sn} values occur are different for each river: in rivers 1 and 3, the maximum k_{sn} values occur around 1,300 m.a.s.l., whereas in river 2, they occur at an elevation of 1,500 m. River 4 shows highest k_{sn} values at around 1,200 m; in rivers 5 and 6, the k_{sn} peak is located at an elevation around 800 m. For rivers 7 and 8, the k_{sn} versus elevation plot is complicated by changes in channel slope related to the interpreted marine terraces, but highest values occur at around 500 and 700 m, respectively. Despite complications in these patterns due to short, low-gradient segments of the rivers, the main trend of the curves shows a hump-shaped distribution of k_{sn} values along the river profiles.

4.2. Linear Inversion Verification Test and Results

Prior to performing the linear inversion, we investigated the relationship between rock-uplift rates and steepness index values (k_{sn}) to evaluate whether there is a linear relationship between these parameters (Figure 5), which would support the assumption implicit in the inversion that the channel slope exponent, n, equals one. To do so, we compare rock-uplift rates associated with individual marine terraces derived from Racano et al. (2020) with the average k_{sn} calculated for the best-fit θ_{ref} of 0.3 in the elevation bands of the terraces (Figure 4b). As noted in the Methods section, if $n = 1$, the vertical movement of steepened sections of the channel will track with vertical movement of the marine terraces (Niemann et al., 2001; Perron & Royden, 2013), and the relationship between k_{sn} and rock-uplift rate will be linear (Equation 18). In Figure 5b, the York regression between U and the average k_{sn} implies a K of 3.05×10^{-4} $\mathrm{m}^{0.4}$/yr with an uncertainty of 4.06×10^{-5} $\mathrm{m}^{0.4}$/yr at the 2σ level. Furthermore, the linear distribution of the points in Figure 5b supports the assumption of $n = 1$ and justifies our application of the linear inversion. The accuracy of the inferred erosion coefficient is corroborated by a brute-force estimation of K made by minimizing the misfit between the cumulative rock-uplift history estimated from marine terraces and the cumulative rock-uplift history from river-profile inversion. In that analysis, we find best-fit K values of 2.5×10^{-4} to 3.25×10^{-4} $\mathrm{m}^{0.4}$/yr (Figure S11).

We first tested the inversion on different sets of rivers within each basin by applying the inversion to basins 5 and 7, where the rock-uplift trend is well documented by the modeling of marine terraces (Racano et al., 2020). Those tests reveal that including all the tributaries in the inversion leads to a large degree of scatter that the inversion does not effectively capture, probably due to (a) some spatial variability in rock-uplift rates within the basin, with peak rock-uplift rates near the coast lower than those in the headwaters, (b) divide migration and river capture, or (c) a poorly constrained $\mathbf{U_{pri}}$ (Figures S2–S8). That scatter leads to a poor match to the trunk streams and underestimates the peak rock-uplift rate that the main streams appear to record. To better capture the magnitude of peak rock-uplift rates recorded by the trunk streams, we performed the linear inversions selecting within the 8 selected basins the main channels oriented approximately perpendicular to the coast that drain from the paleosurface atop the CAP southern margin to the Mediterranean Sea (Figure 6).

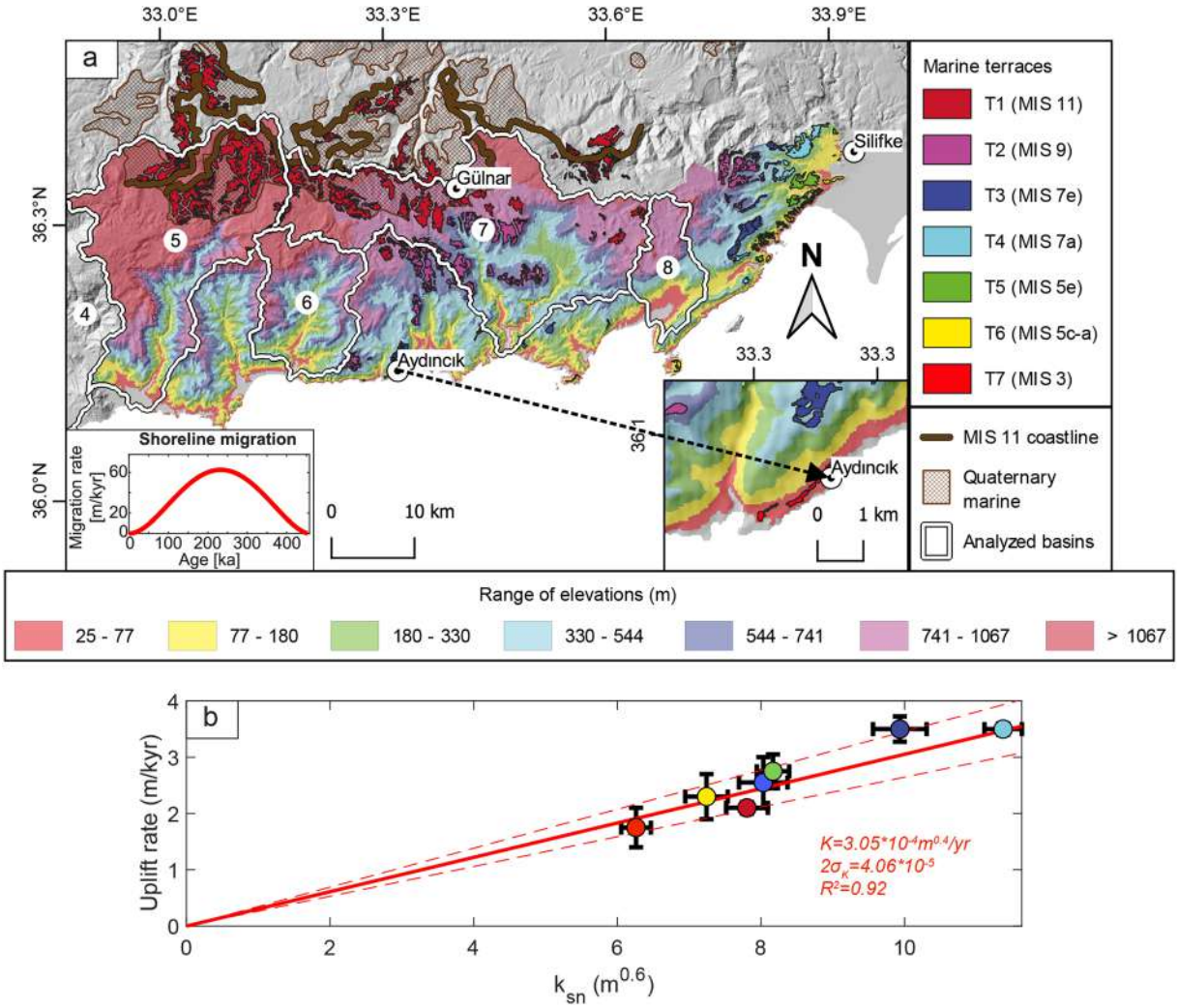

Figure 5. (a) Map of marine terraces and Quaternary marine units atop the CAP southern margin (from Öğretmen, Cipollari, et al., 2018; Racano et al., 2020) and elevation-bands used for the estimation of the average k_{sn} at the level of marine terraces and shoreline migration rate estimated for the last 450 ka; (b) K estimation from the York regression forced through the origin of the average k_{sn} from the marine terrace elevation ranges versus U.

The inverse modeling results show time-variable rock-uplift trends that can be split into a first phase of decreasing rock-uplift rates followed by a fast and strong rock-uplift pulse occurring sometime between 450 and 200 ka. Some differences are evident between the western basins (1, 2, 3, and 4) and the eastern basins (5, 6, 7, and 8). For the western basins, the initial rock-uplift rate (at 700–800 ka) is estimated at ca. 2 m/kyr and is almost constant until 600 ka (Figure 6). After 600 ka, all the western rivers record a strong rock-uplift pulse, where the rock-uplift rate drastically increases to between 6.2 and 8.1 m/kyr over a time window of 200–300 kyr, with increasing rates until ca. 350–450 ka. Subsequently, the rock-uplift rates decrease to between 0.5 and 2 m/kyr at $\tau = 0$ (today). For the eastern basins (5–8), during the first half of the inferred history (from 800 to 500 ka), the rock-uplift rates and trends are similar to those from the western rivers, but the start of the rapid rock-uplift pulse is later, at ca. 500 ka. The peaks in rock-uplift rates also occur later, between 200 and 300 ka. The maximum rock-uplift rates of the eastern rivers are lower than the western ones, at ca. 4.5–5.9 m/kyr for basins 5, 6, and 8, and ca. 3.2 m/kyr for river 7. The anomalously low peak rock-uplift rate for basin 7 likely relates to the poor fit of the river profiles by the inversion, and in particular the insufficiently steep slopes in the inversion result between ca. 200 and 800 m a.s.l (Figure 6). At $\tau = 0$, the rock-uplift rates obtained are similar to the western basins (0.5–1.7 m/kyr). Changing the value of K by

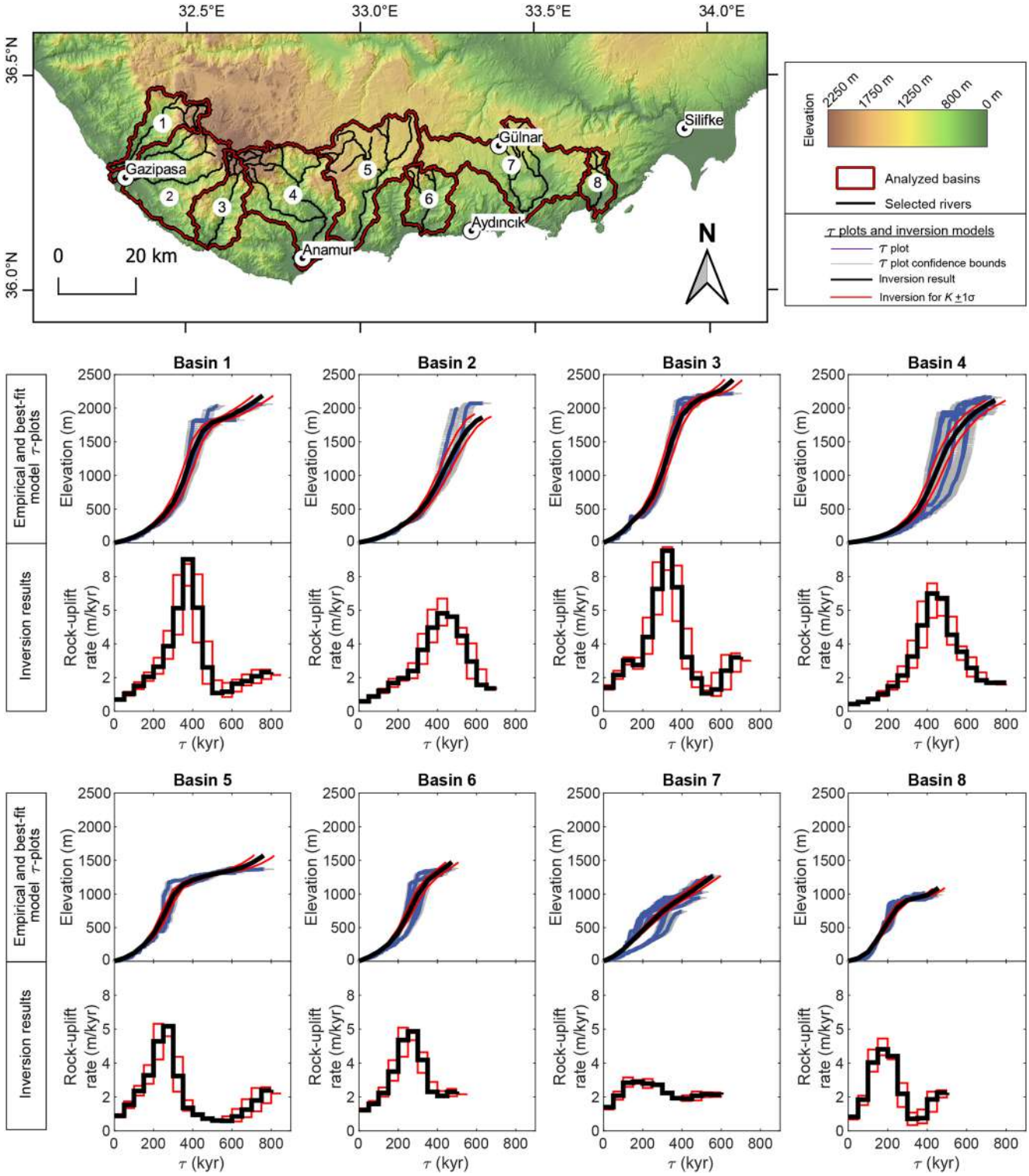

Figure 6. Linear inversions of the main streams of each selected basin with channel heads on the top of the margin. Blue lines indicate the τ-plots of the inverted rivers, gray shade represents the confidence bounds of the τ-plots estimated for $K \pm 1\sigma$ (one standard deviation estimated from the York linear regression). The river-profile inversion has been performed for a time-step of 50 kyr (see Supporting Information). The black curves in τ-plots and the uplift history (inversion results) show the result for the mean value of K estimated in Figure 5b, and the red curves show the results obtained using $K \pm 1\sigma$.

$\pm 2.03 \times 10^{-5}$ $m^{0.4}$/yr (the 1σ uncertainty range) yields results with small shifts in time (sometimes resulting in different numbers of time-steps) and in rock-uplift rates, but does not change the general temporal pattern of rock uplift, nor the spatio-temporal pattern of peak rock-uplift rates occurring earlier in the western basins than in the eastern basins (Figure 6). Even with much larger variations in K, these patterns remain the same (Supporting Information).

5. Discussion

5.1. Rock-Uplift History From Regional Morphology and River-Profile Inversions

Following the work of Goren et al. (2014), if (a) a linear relationship exists between the steepness index (k_{sn}) and the rock-uplift rate, (b) rock-uplift rates are uniform in space, and (c) the erosion coefficient (K) is uniform in space and unchanging in time, then spatial variations in k_{sn} can be related directly to temporal variations in rock-uplift rates. River long profiles that cross the CAP southern margin are marked by major knickpoints, showing a dramatic downstream increase in k_{sn} values, starting near the upper parts of the channel profiles, at around 2,000 m.a.s.l. in the west and around 1,000 m.a.s.l. in the east. These k_{sn} increases can be related to the strong increase in rock-uplift rates that occurred during the Quaternary based on uplifted middle Pleistocene marine sediments (Öğretmen, Cipollari, et al., 2018). The increase in k_{sn} values subsequently decreases rapidly farther downstream, following a bell-shape trend. If interpreted in terms of a rock-uplift history, these channel profiles indicate a rapid increase in rock-uplift rates followed by a subsequent rapid decrease. These interpretations are qualitatively consistent with the rock-uplift history derived by modeling of marine terrace evolution (Racano et al., 2020).

However, our analysis of the morphology of the regional landscape suggests probable west-to-east variations in the rock-uplift history along the southern CAP margin. Mean slope values on hillslopes, the eastward tilt of the paleosurface that caps the margin, the eastward decrease in elevations of the major knickpoints, and mean k_{sn} values are all consistent with higher rock uplift in the west compared to the east. The west-to-east decrease in k_{sn} along the plateau margin is independent from the main eroded lithologies (that pass from mainly metamorphic rocks in the west to sedimentary rocks to the east) and shows a trend that is opposite of that expected from the minor decrease in precipitation toward the east (drier regions are expected to show steeper slopes for a given rock-uplift rate and erosion coefficient; D'Arcy & Whittaker, 2014). These observations support our inference that the rock-uplift history is the primary factor that has affected the river profile shapes in the region.

River-profile inversions applied to individual river basins allowed us to obtain quantitative estimates of the Quaternary rock-uplift history. But rather than obtaining a single estimate for the rock-uplift history, the set of rivers spanning the west-east extent of the margin allow us to also investigate possible west-to-east spatial variations in rock-uplift histories.

The first main result regarding the linear inversion regards the estimation of K. The linearity between rock-uplift rate and k_{sn} justifies the application of the linear inversion model (e.g., Quye-Sawyer et al., 2020) and allows us to estimate the erosion coefficient from the relationship between k_{sn} and rock-uplift rate (Figure 5b). Incidentally, that correlation between rock-uplift rate and k_{sn} also supports our assumption of detachment-limited behavior of the channels, as gravel-bedded channels are instead expected to show correlations between rock-uplift rate and concavity (Wickert & Schildgen, 2019).

Based on our estimate of K, our inversion results yield rock-uplift histories that span a time range between 800 ka and the present. However, these results need to be interpreted taking into account the geology of the area, and in particular the Quaternary marine phase that affected the eastern side of the CAP southern margin until the middle Pleistocene. The analysis of calcareous plankton and benthic fauna performed by Öğretmen, Cipollari, et al. (2018) and Öğretmen, Frezza, et al. (2018) in the marine sediments atop the plateau margin reveals that the area experienced marine deposition until 470 ka. The results of the river-profile inversion are inconsistent with the age of the marine sediments, because they include a history of the drainage system older than the end of marine sedimentation. We shade out that region in Figure 7 to indicate that portion should not be considered. However, the western side of the plateau margin lacks Quaternary marine sediments, and the preserved coastline on top of the eastern plateau margin (Öğretmen, Cipollari,

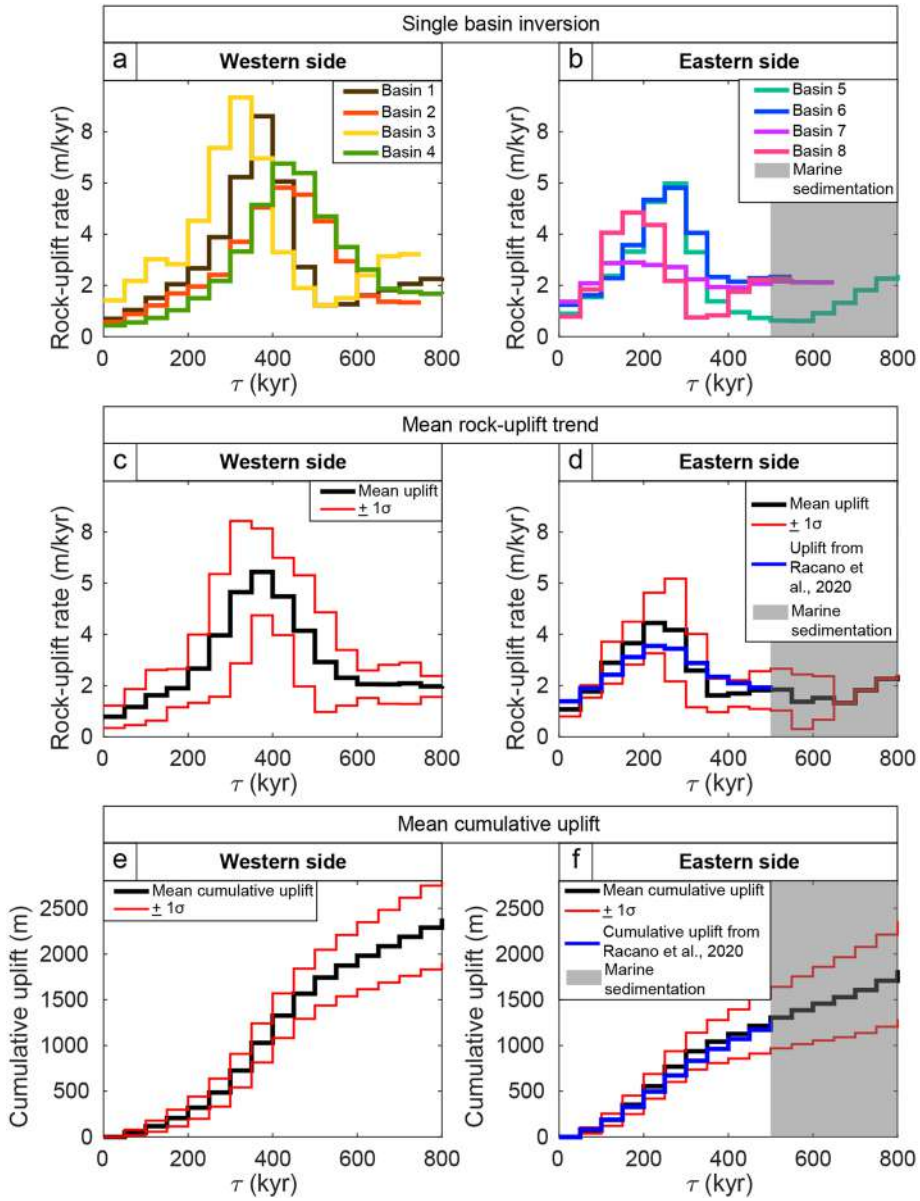

Figure 7. Rock-uplift histories for selected rivers (a and b), mean rock-uplift trend (c and d), cumulative uplift (e and f), and one standard deviation ($\pm 1\sigma$) uncertainty range (in red) estimated for the western (c) and eastern (d) sides of the study area. Blue line in (d and f) shows the surface uplift-trend and the cumulate uplift inferred for a time step of 50 kyr from Racano et al. (2020) on the eastern side of the Central Anatolian Plateau southern margin based on marine-terrace modeling. The gray box indicates the marine deposition phase in the eastern side of the plateau (Öğretmen, Cipollari, et al., 2018; Öğretmen, Frezza, et al., 2018), where the uplift history derived from the inversion should be ignored.

et al., 2018; Racano et al., 2020) suggests that the western area remained above sea-level during the Quaternary. In this case, the reconstructed rock-uplift history could be considered reliable for the whole period, assuming that (a) the drainage divides remained stable (discussed below) and (b) Equation 17 provides a reasonable constraint on the $\mathbf{U_{pri}}$ in the river inversion (see Figures S6, S7 and S8). Considering that a continental paleolandscape existed prior to the Quaternary rock-uplift pulse, the low-gradient upper portion of the river profiles may reliably approximate the pre-uplift, relict landscape.

The inferred rock-uplift histories from the western and eastern basins show a bell-shaped trend for the middle to late Pleistocene. However, the peak rock-uplift rates differ in timing and magnitude between

the western and the eastern sides of the plateau margin. In the west, the start of the increased rock-uplift rates occurs around 600 ka, and the peak rates occur around 400 ka, reaching up to ca. 4.9–9.2 m/kyr and about 2,500 m of cumulate rock uplift (Figures 7a, 7c and 7e). In the east, the rock-uplift pulse starts later, around 400 ka, and the peak rates occur at ca. 250 ka, with maximum rock-uplift rates of 3.0–5.1 m/kyr (or 4.5–5.1 m/kyr, excluding Basin 7) (Figures 7b and 7d). These inferred rock-uplift histories from the river-profile inversions are similar to the mean rock-uplift history obtained by modeling marine terraces from the CAP southern margin, which are located within the drainage basins of rivers 5, 6, 7, and 8 (Racano et al., 2020). For those eastern basins, the marine terrace rock-uplift history lies within the uncertainty bounds of the rock-uplift history obtained by river-profile inversion (Figure 7d). The cumulative rock uplift inferred from river-profile inversion is also similar to the cumulative rock uplift from modeled marine terraces (Figure 7f). We argue that there is no circularity in this comparison of the two histories, even though the erosion coefficient K is calibrated from the marine terrace record, because the calibration only determines the relationship between local channel gradients and rock-uplift rate, not the shape of the rock-uplift curve. This agreement between the rock-uplift history derived from marine-terrace modeling and that derived from our river-profile inversion provides additional support for our initial inference that the slope exponent, n, is indistinguishable from 1.

Our results showing that western basins record earlier peak rock-uplift times and higher peak rock-uplift rates (Figure 7) are robust; applying K values lower or higher than 3.05×10^{-4} $m^{0.4}$/yr uniformly along the plateau margin changes the absolute timing of rock uplift, but not the relative timing between the western and eastern sides (Supporting Information), supporting our inference that the rock-uplift pulse affected first the western side of the plateau margin and moved eastward through time. However, differences in lithology could result in spatial variations in K between the western (1–4) and eastern (5–8) drainage basins. Unfortunately, no useful constraints are available to estimate independently the erosion coefficient for the western basins. Nevertheless, if the western basins had a lower erosion coefficient compared to the eastern basins, as one may expect given the greater prevalence of metamorphic rocks, the timing of rock uplift in the west would be even older than we have estimated. Hence, the potential spatial variations in K that one might expect based on the mapped geology would not affect our interpretation that the peak rock-uplift pulse proceeded from west to east through time.

The dependency of the response time on the erosion coefficient K (Equation 12) is also illustrated by comparing our results to those of McNab et al. (2018). Although that study performed river-profile inversions over a much larger region, their results from the southern margin of the CAP show similarities with the results here, with rock uplift starting earlier in the western basins compared to the eastern basins (Figures 6a and 6f in McNab et al., 2018). An important difference between that study and ours is that McNab et al. (2018) used the late Miocene marine sediments atop the southern CAP margin, rather than the more recently described middle Pleistocene marine sediments (Öğretmen, Cipollari, et al., 2018) and marine terraces (Racano et al., 2020), to perform their calibration of K. This difference results in a much lower K value in the McNab et al. (2018) inversions, resulting in slower inferred rock-uplift rates and much more prolonged rock-uplift histories. For example, faster rock uplift of the western basins from McNab et al. (2018) starts at ca. 6–5 Ma, whereas in our inversion, it starts at ca. 400–500 ka.

5.2. Effects of Changes in Channel Length on River-Profile Inversions

The formation of marine terraces during rock uplift implies a seaward migration of the shoreline through time (Figure 5a). However, the calculation of the integral τ assumes a steady-state position of the basin outlet through time. The effect of shoreline migration would be to lengthen the river profile, causing the rock-uplift history inferred by the τ plot for the upstream reaches to shift further back in time compared to a scenario with no shoreline migration. However, the good agreement of the rock-uplift trend inferred by marine terrace analysis (Racano et al., 2020) and the rock-uplift trend obtained by river-profile inversion in the same region as the marine terraces suggests that the effects of shoreline migration on the inversion results are negligible. This finding could imply that any shoreline migration that occurred was minor, which seems reasonable considering the steep slopes in the region. Considering that the coast becomes even steeper going westward, we can assume that the magnitude of shoreline migration was even lower (and hence, less important) in the west. However, if shoreline migration had the effect of making the timing of apparent

rock uplift look older, then the timing in the east has been made to look artificially older more so than in the west. Thus, any effect of shoreline migration does not alter the conclusion that the uplift pulse was earlier in the west than in the east.

Shifts in the drainage divides could also change the channel length and affect the results of the river-profile inversions. Specifically, lengthening at the upstream end will cause newly added portions of the drainage network to have high τ values, which we may then incorrectly interpret as reflecting the earliest portion of the rock-uplift history. Also, the added drainage area will decrease τ values downstream, causing the overall rock-uplift history to shift to more recent times. For the western basins in particular, hillslope values, local relief, and k_{sn} values suggest that drainage divides between the Göksu basin (on the low-relief upper surface) and the south-draining catchments (basins 1–4) are unstable, with divides that should have a tendency to migrate north or northeastward toward the Göksu basin. However, similar to our argument concerning shoreline migration, the contribution of gradual divide migration is unlikely to be important for our results because basin lengthening over the past ca. 500 kyr would likely be minor (ca. 2 km; see Supporting Information) along the steep plateau margins. An increase in area in the west would decrease τ for a given point on the river, making the rock-uplift timing apparently younger than it should be. If divide migration were significant, since it only seems likely to have affected the western basins, the timing of uplift in those basins could be older than it appears in our inversions. The result would still be consistent with west-to-east propagation of the rock-uplift pulse. In the Supporting Information, we use a quantitative test for drainage capture, following the methods of Giachetta and Willett (2018), and explore the impact of potential capture on river-profile inversions. Although there is some evidence for capture in a sub-set of the drainage basins (Basins 1, 4, and 6), the inferred timing of the peak rock-uplift rate is insignificantly different in models in which the potentially captured channels and their upstream areas are removed versus models of the existing basins (Figures S4 and S5).

5.3. Spatial Variations in CAP Southern Margin Uplift and Uplift Mechanism

The first evident geomorphological feature of the CAP southern margin is the eastward tilt of the present-day plateau-margin topography. Our river-profile analysis reveals that this tilt can be explained through differential rock uplift of the western and eastern sides of the margin during the middle Pleistocene. Based on our river-profile inversions, the western side of the margin experienced a peak in rock-uplift rates 100–200 kyr earlier than the eastern side, and the mean rock-uplift rate is faster (mean of ca. 5.1 m/kyr on the western side vs. 4.2 m/kyr on the eastern side, Figures 7c and 7d).

Different mechanisms have been invoked to explain the topography that has developed at the CAP southern margin, including slab break-off (Cosentino et al., 2012; Öğretmen, Cipollari, et al., 2018; Schildgen, Cosentino, Bookhagen, et al, 2012; Schildgen, Cosentino, Caruso, et al, 2012; Schildgen et al, 2014), removal of lithospheric mantle and crustal thickening (Meijers et al., 2018), continental collision (McPhee & van Hinsbergen, 2019) and thermal-viscous deformation of the crust (Fernández-Blanco et al., 2019, 2020). However, mechanisms like crustal underplating or thermal-viscous deformation (Fernández-Blanco et al., 2019, 2020; Meijers et al., 2018) estimate maximum rock-uplift rates between 0.4 and 0.7 m/kyr (Fernández-Blanco et al., 2019, 2020; Meijers et al., 2018). As a result, they cannot account for the very rapid rock-uplift rates, with peaks exceeding 3 m/kyr, that have occurred during the middle Pleistocene, which are supported by biostratigrpahic results on uplifted marine sediments (Öğretmen, Cipollari, et al., 2018), marine-terrace modeling (Racano et al., 2020), and the river-inversion results presented here. Considering that geodynamic models suggest slab break-off can trigger rock-uplift rates in the overriding plate of up to 7–9 m/kyr over very short time windows of ca. 100 ky (Duretz & Gerya, 2013; Magni et al., 2017), the mechanism that best fits with the rock-uplift history and landscape evolution at the CAP southern margin is break-off of the subducting slab (Figure 8).

Based on modeling uplift of the southeastern Carpathian chain, Göğüş et al. (2016) proposed that lithospheric delamination can generate brief periods of rapid rock uplift (6 km in ca. 1.2 Myr) both with and without slab break-off. However, to invoke such a mechanism to explain the uplift history of the southern CAP would require delamination to propagate in a direction perpendicular to the convergence direction, that is, along strike of the slab from west to east. Such a propagation direction would be at odds with delamination that is driven by roll-back of the slab, which would be perpendicular to the strike of the subduction

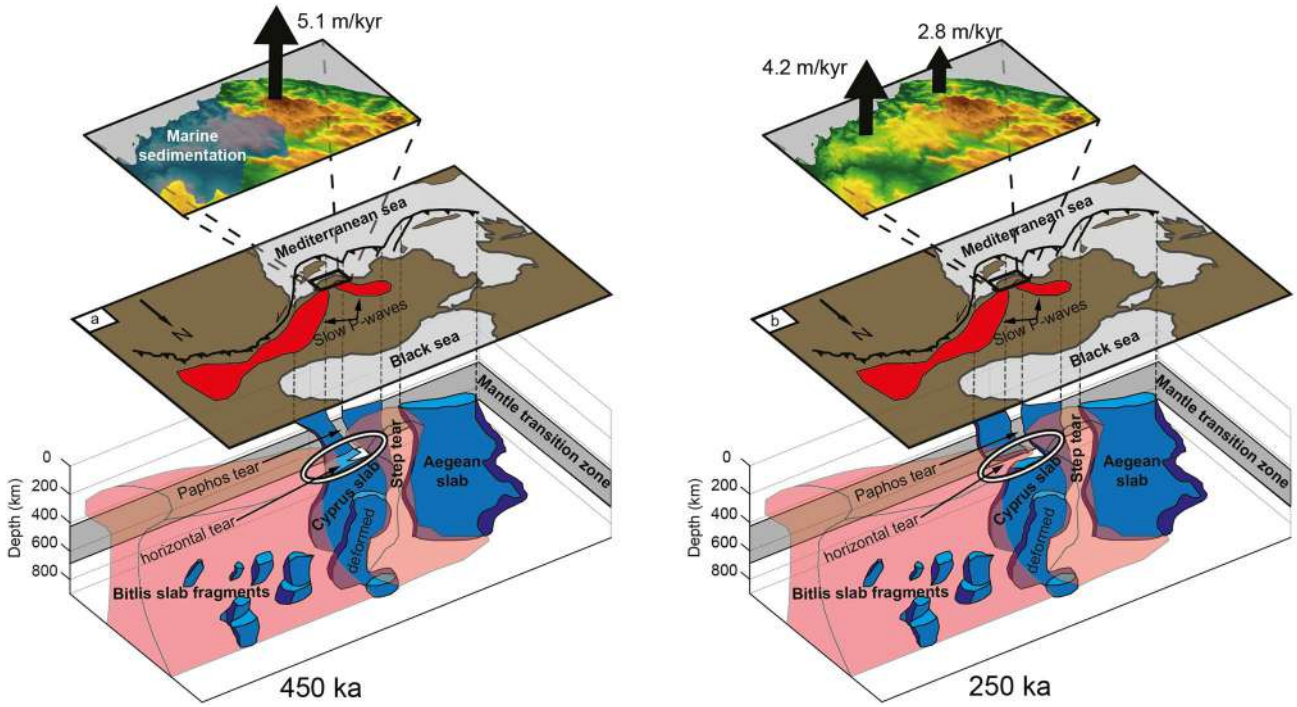

Figure 8. Schematic illustration of upwelling asthenosphere through a lithospheric slab break and tear (modified from Schildgen, Cosentino, Caruso, et al., 2012; geometry of slabs from Portner et al., 2018), with map above showing regions of low Pn-wave velocities in red (Gans et al., 2009) and the differential rock-uplift rates related to the Quaternary topographic growth of the Central Anatolian Plateau southern margin. White circles highlight the portion of the Cyprus slab that we infer to have torn since the middle Pleistocene, driving a west-to-east propagating pulse of rapid rock-uplift.

zone. Also, the spatially restricted nature of the uplift pulse would require a narrow strip of lithosphere to delaminate. For these reasons, even if delamination may produce rock-uplift rates similar to what we find from the river-profile inversions, we do not consider delamination to be a viable mechanism to explain the rock-uplift patterns we reconstruct.

Other characteristics of the subducting slabs, such as slab tears orthogonal to the trench, may have influenced the rock-uplift history of the CAP southern margin. Low velocity anomalies between the Aegean and Cyprus slabs (Bakırcı et al., 2012; Biryol et al., 2011; Kounoudis et al., 2020; Portner et al., 2018; Salaün et al., 2012), differences in GPS-derived velocity vectors (Barka & Reilinger, 1997) and earthquake focal mechanisms (Özbakır et al., 2013) have been used to suggest a tear with upwelling asthenosphere between the Cyprus and Aegean slabs. If this slab tear is responsible for the west-to-east differences in rock-uplift histories along the CAP southern margin, then the orthogonal tear is likely a recent (i.e., middle Pleistocene) feature of the subducting slab, which was followed shortly by break-off of the Cyprus slab. Alternatively, the west-to-east variation in the rock-uplift history may result from a west-to-east propagation of slab tearing within the Cyprus slab. In their recent tomography, Portner et al. (2018) show a tear in the eastern portion of the Cyprus slab, beneath our study region, but no tear in the western portion of the slab (to the west of our westernmost analyzed drainage basin) (Figure 8). A west-to-east propagation direction for a break-off in the Cyprus slab would thus imply that the Cyprus slab is cut by a tear in the trench-orthogonal direction, as was inferred in the tomography by Biryol et al. (2011), and could be corroborated by the existence of the Paphos transform fault, which separates the trenches associated with each portion of the slab.

6. Conclusions

Qualitative analysis of the southern CAP margin morphology combined with linear inversions of river profiles draining the southern flank of the margin reveal that the Quaternary rock-uplift pulse responsible for km-scale growth of the plateau margin was variable in space and time. An overall eastward tilt of the margin is defined by the eastward dip of the margin-capping planar surface, a west-to-east decrease in the

elevation of the knickpoints that mark the edge of the surface, and a west-to-east decrease in topographic gradients and river steepness values. From a qualitative river-profile analyses, we argue that along-channel variations in k_{sn} values indicate that rock-uplift rates increased and then decreased through time. Quantitatively, our linear inversion of river profiles yielded uplift histories that are comparable with the rock-history obtained by terrace-evolution modeling of marine terraces along the eastern sector of the southern CAP margin (Racano et al., 2020). The river-profile inversion also revealed differences in the timing and rates of the Quaternary rock-uplift pulse between the western and the eastern sides of the CAP southern margin: on the western side, the estimated age of the rock-uplift peak is around 400 ka, with instantaneous rock-uplift rates of up to 6.1 m/kyr, whereas on the eastern side, the peak rock uplift is recorded at 250 ka with rates of 4.3 m/kyr. The differences in rock-uplift histories are consistent with the current eastward tilt of the plateau margin. Together, the temporal pattern of the rock-uplift rates and the inferred magnitude of rock-uplift rates are consistent with crustal rebound following slab break-off during the Pleistocene, with lateral variations in the rock-uplift history likely resulting from eastward migration of a tear in the Cyprus slab and/or enhanced mantle upwelling between the Cyprus and Aegean slabs prior to break-off of the Cyprus slab.

Data Availability Statement

Data used in the paper include digital elevation data from the Shuttle Radar Topography Mission, available for free download at https://earthexplorer.usgs.gov. The code used to run perform the linear inversion is available at https://zenodo.org/record/4317965#.YGSdAK9KiLK (Gallen, 2020).

Acknowledgments
The grant to Dipartimento di Scienze, Università degli Studi Roma Tre (MIUR-Italy Dipartimenti di Eccellenza, articolo 1, commi 314–337 legge 232/2016) is gratefully acknowledged for support of S. Racano. The authors also gratefully acknowledge the Helmholtz-Zentrum Potsdam—Deutsches GeoForschungsZentrum (GFZ)—Section 4.6 (Geomorphology) for the financial support given to complete the research. The authors thank the Associate Editor and reviewers M. Fox, S. Gallen, and O. Göğüş for their constructive comments and suggestions that helped us to significantly improve the study.

References

Aksu, A. E., Calon, T. J., Hall, J., Mansfield, S., & Yaşar, D. (2005). The Cilicia-Adana basin complex, Eastern Mediterranean: Neogene evolution of an active fore-arc basin in an obliquely convergent margin. *Marine Geology*, *221*(1), 121–159. https://doi.org/10.1016/j.margeo.2005.03.011

Aksu, A. E., Walsh-Kennedy, S., Hall, J., Hiscott, R. N., Yaltırak, C., Akhun, S. D., & Çifçi, G. (2014). The Pliocene-Quaternary tectonic evolution of the Cilicia and Adana basins, eastern Mediterranean: Special reference to the development of the Kozan Fault zone. *Tectonophysics*, *622*, 22–43. https://doi.org/10.1016/j.tecto.2014.03.025

Aydar, E., Çubukçu, H., Şen, E., & Akın, L. (2013). Central Anatolian Plateau, Turkey: Incision and paleoaltimetry recorded from volcanic rocks. *Turkish Journal of Earth Sciences*, *22*(5), 739–746. https://doi.org/10.3906/sag-1203-7210.3906/yer-1211-8

Bakırcı, T., Yoshizawa, K., & Özer, M. F. (2012). Three-dimensional S-wave structure of the upper mantle beneath Turkey from surface wave tomography: 3-D upper-mantle structure beneath Turkey. *Geophysical Journal International*, *190*(2), 1058–1076. https://doi.org/10.1111/j.1365-246X.2012.05526.x

Ballato, P., Uba, C. E., Landgraf, A., Strecker, M. R., Sudo, M., Stockli, D. F., et al. (2011). Arabia-Eurasia continental collision: Insights from late tertiary foreland-basin evolution in the Alborz Mountains, northern Iran. *The Geological Society of America Bulletin*, *123*(1–2), 106–131. https://doi.org/10.1130/B30091.1

Barka, A., & Reilinger, R. (1997). Active tectonics of the Eastern Mediterranean region: Deduced from GPS, neotectonic and seismicity data. *Annals of Geophysics*, *40*(3). https://doi.org/10.4401/ag-3892

Barka, A. A., & Kadinsky-Cade, K. (1988). Strike-slip fault geometry in Turkey and its influence on earthquake activity. *Tectonics*, *7*(3), 663–684. https://doi.org/10.1029/TC007i003p00663

Bartol, J., & Govers, R. (2014). A single cause for uplift of the Central and Eastern Anatolian plateau? *Tectonophysics*, *637*, 116–136. https://doi.org/10.1016/j.tecto.2014.10.002

Berndt, C., Yıldırım, C., Çiner, A., Strecker, M. R., Ertunç, G., Sarıkaya, M. A., et al. (2018). Quaternary uplift of the northern margin of the Central Anatolian Plateau: New OSL dates of fluvial and delta-terrace deposits of the Kızılırmak River, Black Sea coast, Turkey. *Quaternary Science Reviews*, *201*, 446–469. https://doi.org/10.1016/j.quascirev.2018.10.029

Biryol, C., Beck, S. L., Zandt, G., & Özacar, A. A. (2011). Segmented African lithosphere beneath the Anatolian region inferred from teleseismic P-wave tomography: Segmented lithosphere beneath Anatolia. *Geophysical Journal International*, *184*(3), 1037–1057. https://doi.org/10.1111/j.1365-246X.2010.04910.x

Burke, K., & Sengör, C. (1986). Tectonic escape in the evolution of the continental crust. In M. Barazangi, & L. Brown (Eds.), *Geodynamics Series*. (Vol. 14, pp. 41–53). American Geophysical Union. https://doi.org/10.1029/GD014p0041

Büyüksaraç, A., Jordanova, D., Ateş, A., & Karloukovski, V. (2005). Interpretation of the gravity and magnetic anomalies of the Cappadocia region, Central Turkey. *Pure and Applied Geophysics*, *162*(11), 2197–2213. https://doi.org/10.1007/s00024-005-2712-9

Çiner, A., Doğan, U., Yıldırım, C., Akçar, N., Ivy-Ochs, S., Alfimov, V., et al. (2015). Quaternary uplift rates of the Central Anatolian Plateau, Turkey: Insights from cosmogenic isochron-burial nuclide dating of the Kızılırmak River terraces. *Quaternary Science Reviews*, *107*, 81–97. https://doi.org/10.1016/j.quascirev.2014.10.007

Çolakoğlu, A. R., & Arehart, G. B. (2010). The petrogenesis of Sarıçimen (Çaldıran-Van) quartz monzodiorite: Implication for initiation of magmatism (late Medial Miocene) in the east Anatolian collision zone, Turkey. *Lithos*, *119*(3), 607–620. https://doi.org/10.1016/j.lithos.2010.08.014

Cosentino, D., Schildgen, T. F., Cipollari, P., Faranda, C., Gliozzi, E., Hudackova, N., et al. (2012). Late Miocene surface uplift of the southern margin of the Central Anatolian Plateau, Central Taurides, Turkey. *The Geological Society of America Bulletin*, *124*(1–2), 133–145. https://doi.org/10.1130/B30466.1

D'Arcy, M., & Whittaker, A. C. (2014). Geomorphic constraints on landscape sensitivity to climate in tectonically active areas. *Geomorphology*, *204*, 366–381. https://doi.org/10.1016/j.geomorph.2013.08.019

Dewey, J. F., & Şengör, A. M. C. (1979). Aegean and surrounding regions: Complex multiplate and continuum tectonics in a convergent zone. *The Geological Society of America Bulletin*, *90*(1), 84. https://doi.org/10.1130/0016-7606(1979)90<84:aasrcm>2.0.co;2

Duretz, T., & Gerya, T. V. (2013). Slab detachment during continental collision: Influence of crustal rheology and interaction with lithospheric delamination. *Tectonophysics*, *602*, 124–140. https://doi.org/10.1016/j.tecto.2012.12.024

Ehlers, T. A., & Poulsen, C. J. (2009). Influence of Andean uplift on climate and paleoaltimetry estimates. *Earth and Planetary Science Letters*, *281*(3–4), 238–248. https://doi.org/10.1016/j.epsl.2009.02.026

Ekici, T. (2016). Collision-related slab break-off volcanism in the Eastern Anatolia, Kepez volcanic complex (Turkey). *Geodinamica Acta*, *28*(3), 223–239. https://doi.org/10.1080/09853111.2015.1121796

Faccenna, C., Bellier, O., Martinod, J., Piromallo, C., & Regard, V. (2006). Slab detachment beneath eastern Anatolia: A possible cause for the formation of the North Anatolian fault. *Earth and Planetary Science Letters*, *242*(1–2), 85–97. https://doi.org/10.1016/j.epsl.2005.11.046

Fernández-Blanco, D., Bertotti, G., Aksu, A., & Hall, J. (2019). Monoclinal flexure of an orogenic plateau margin during subduction, south Turkey. *Basin Research*, *31*(4), 709–727. https://doi.org/10.1111/bre.12341

Fernández-Blanco, D., Mannu, U., Bertotti, G., & Willett, S. D. (2020). Forearc high uplift by lower crustal flow during growth of the Cyprus-Anatolian margin. *Earth and Planetary Science Letters*, *544*, 116–314. https://doi.org/10.1016/j.epsl.2020.116314

Flint, J. J. (1974). Stream gradient as a function of order, magnitude, and discharge. *Water Resources Research*, *10*(5), 969–973. https://doi.org/10.1029/WR010i005p00969

Forte, A. M., & Whipple, K. X. (2019). Short communication: The Topographic Analysis Kit (TAK) for TopoToolbox. *Earth Surface Dynamics*, *7*, 87–95. https://doi.org/10.5194/esurf-7-87-2019

Fox, M., Goren, L., May, D. A., & Willett, S. D. (2014). Inversion of fluvial channels for paleorock uplift rates in Taiwan. *Journal of Geophysical Research: Earth Surface*, *119*(9), 1853–1875. https://doi.org/10.1002/2014JF003196

Fox, M., Leith, K., Bodin, T., Balco, G., & Shuster, D. L. (2015). Rate of fluvial incision in the Central Alps constrained through joint inversion of detrital ^{10}Be and thermochronometric data. *Earth and Planetary Science Letters*, *411*, 27–36. https://doi.org/10.1016/j.epsl.2014.11.038

Gallen, S. F. (2018). Lithologic controls on landscape dynamics and aquatic species evolution in post-orogenic mountains. *Earth and Planetary Science Letters*, *493*, 150–160. https://doi.org/10.1016/j.epsl.2018.04.029

Gallen, S. F. (2020). *sfgallen/Block_Uplift_Linear_Inversion_Models: Block uplift linear inversion v1 (Version block_uplift_inversion)*. Zenodo. https://doi.org/10.5281/zenodo.4317965

Gans, C. R., Beck, S. L., Zandt, G., Biryol, C. B., & Ozacar, A. A. (2009). Detecting the limit of slab break-off in central Turkey: New high-resolution Pn tomography results. *Geophysical Journal International*, *179*(3), 1566–1572. https://doi.org/10.1111/j.1365-246X.2009.04389.x

Giachetta, E., & Willett, S. D. (2018). A global dataset of river network geometry. *Scientific Data*, *5*, 180127. https://doi.org/10.1038/sdata.2018.127

Göğüş, O. H., Pysklywec, R. N., & Faccenna, C. (2016). Postcollisional lithospheric evolution of the Southeast Carpathians: Comparison of geodynamical models and observations. *Tectonics*, *35*, 1205–1224. https://doi.org/10.1002/2015TC004096

Göğüş, O. H., Pysklywec, R. N., Şengör, A. M. C., & Gün, E. (2017). Drip tectonics and the enigmatic uplift of the Central Anatolian Plateau. *Nature Communications*, *8*(1), 1538. https://doi.org/10.1038/s41467-017-01611-3

Goren, L., Fox, M., & Willett, S. D. (2014). Tectonics from fluvial topography using formal linear inversion: Theory and applications to the Inyo Mountains, California. *Journal of Geophysical Research: Earth Surface*, *119*(8), 1651–1681. https://doi.org/10.1002/2014JF003079

Gregory-Wodzicki, K. M. (2000). Uplift history of the central and northern Andes: A review. *GSA Bulletin*, *112*(7), 1091–1105. https://doi.org/10.1130/0016-7606(2000)112<1091:UHOTCA>2.0.CO;2

Güneş, P., Aksu, A. E., & Hall, J. (2018). Internal seismic stratigraphy of the Messinian evaporites across the northern sector of the eastern Mediterranean Sea. *Marine and Petroleum Geology*, *91*, 297–320. https://doi.org/10.1016/j.marpetgeo.2018.01.016

Hack, J. T. (1957). *Studies of longitudinal stream profiles in Virginia and Maryland. Shorter contributions to general geology* (Vol. 294, pp. 45–97). US Government Printing Office. https://doi.org/10.3133/pp294b

Hack, J. T. (1960). *Interpretation of erosional topography in humid temperate regions. American Journal of Science*. Bobbs-Merrill.

Harkins, N., Kirby, E., Heimsath, A., Robinson, R., & Reiser, U. (2007). Transient fluvial incision in the headwaters of the Yellow River, northeastern Tibet, China. *Journal of Geophysical Research*, *112*. https://doi.org/10.1029/2006JF000570

Harris, N. (2006). The elevation history of the Tibetan Plateau and its implications for the Asian monsoon. *Palaeogeography, Palaeoclimatology, Palaeoecology*, *241*(1), 4–15. https://doi.org/10.1016/j.palaeo.2006.07.009

Hartley, A. (2003). Andean uplift and climate change. *Journal of the Geological Society*, *160*(1), 7–10. https://doi.org/10.1144/0016-764902-083

Howard, A. D. (1994). A detachment-limited model of drainage basin evolution. *Water Resources Research*, *30*(7), 2261–2285. https://doi.org/10.1029/94WR00757

Howard, A. D., & Kerby, G. (1983). Channel changes in badlands. *GSA Bulletin*, *94*(6), 739–752. https://doi.org/10.1130/0016-7606(1983)94<739:ccib>2.0.co;2

Karaoğlan, F. (2016). Tracking the uplift of the Bolkar Mountains (south-central Turkey): Evidence from apatite fission track thermochronology. *Turkish Journal of Earth Sciences*, *25*(1), 64–80.

Karaoğlan, F., Parlak, O., Hejl, E., Neubauer, F., & Klötzli, U. (2016). The temporal evolution of the active margin along the Southeast Anatolian Orogenic Belt (SE Turkey): Evidence from U-Pb, Ar-Ar and fission track chronology. *Gondwana Research*, *33*, 190–208. https://doi.org/10.1016/j.gr.2015.12.011

Kaymakci, N., Inceöz, M., Ertepinar, P., & Koç, A. (2010). Late Cretaceous to recent kinematics of SE Anatolia (Turkey). *Geological Society, London, Special Publications*, *340*(1), 409–435. https://doi.org/10.1144/SP340.18

Keskin, M. (2003). Magma generation by slab steepening and breakoff beneath a subduction-accretion complex: An alternative model for collision-related volcanism in Eastern Anatolia, Turkey: Model for collision-related volcanism. *Geophysical Research Letters*, *30*(24). https://doi.org/10.1029/2003GL018019

Keskin, M. (2007). Eastern Anatolia: A hotspot in a collision zone without a mantle plume. In G. R. Foulger, & D. M. Jurdy (Eds.), *Special Paper 430: Plates, Plumes and Planetary Processes* (Vol. 430, pp. 693–722). Geological Society of America. https://doi.org/10.1130/2007.2430(32)

Keskin, M., Pearce, J. A., & Mitchell, J. G. (1998). Volcano-stratigraphy and geochemistry of collision-related volcanism on the Erzurum-Kars Plateau, northeastern Turkey. *Journal of Volcanology and Geothermal Research*, *85*(1), 355–404. https://doi.org/10.1016/S0377-0273(98)00063-8

Ketin, I. (1948). Über die tektonisch-mechanischen Folgerungen aus den großen anatolischen Erdbeben des letzten Dezenniums. *Geologische Rundschau*, *36–36*(1), 77–83. https://doi.org/10.1007/BF01791916

Kirby, E., & Whipple, K. X. (2012). Expression of active tectonics in erosional landscapes. *Journal of Structural Geology*, *44*, 54–75. https://doi.org/10.1016/j.jsg.2012.07.009

Kounoudis, R., Bastow, I. D., Ogden, C. S., Goes, S., Jenkins, J., Grant, B., & Braham, C. (2020). Seismic tomographic imaging of the eastern Mediterranean mantle: implications for terminal-stage subduction, the uplift of Anatolia, and the development of the north Anatolian fault. *Geochemistry, Geophysics, Geosystems*, *21*(7). https://doi.org/10.1029/2020GC009009

Lenters, J. D., & Cook, K. H. (1997). On the origin of the Bolivian high and related circulation features of the South American climate. *Journal of the Atmospheric Sciences*, *54*(5), 656–678. https://doi.org/10.1175/1520-0469(1997)054<0656:otootb>2.0.co;2

Li, X., Zhang, H., Wang, Y., Zhao, X., Ma, Z., Liu, K., & Ma, Y. (2020). Inversion of bedrock channel profiles in the Daqing Shan in Inner Mongolia, northern China: Implications for late Cenozoic tectonic history in the Hetao basin and the Yellow River evolution. *Tectonophysics*, *790*, 228558. https://doi.org/10.1016/j.tecto.2020.228558

Lüdecke, T., Mikes, T., Rojay, F. B., Cosca, M. A., & Mulch, A. (2013). Stable isotope-based reconstruction of Oligo-Miocene paleoenvironment and paleohydrology of Central Anatolian lake basins (Turkey). *Turkish Journal of Earth Sciences*, *22*(5), 793–819. https://doi.org/10.3906/yer-1207-11

Ma, Z., Zhang, H., Wang, Y., Tao, Y., & Li, X. (2020). Inversion of Dadu River Bedrock channels for the late Cenozoic uplift history of the Eastern Tibetan Plateau. *Geophysical Research Letters*, *47*(4). https://doi.org/10.1029/2019GL086882

Magni, V., Allen, M. B., van Hunen, J., & Bouilhol, P. (2017). Continental underplating after slab break-off. *Earth and Planetary Science Letters*, *474*, 59–67. https://doi.org/10.1016/j.epsl.2017.06.017

McKenzie, D. (1978). Active tectonics of the Alpine-Himalayan belt: The Aegean Sea and surrounding regions. *Geophysical Journal International*, *55*(1), 217–254. https://doi.org/10.1111/j.1365-246X.1978.tb04759.x

McNab, F., Ball, P. W., Hoggard, M. J., & White, N. J. (2018). Neogene uplift and magmatism of Anatolia: insights from drainage analysis and basaltic geochemistry. *Geochemistry, Geophysics, Geosystems*, *19*(1), 175–213. https://doi.org/10.1002/2017GC007251

McPhee, P. J., Altıner, D., & van Hinsbergen, D. J. J. (2018). First balanced cross section across the Taurides fold-thrust belt: Geological constraints on the subduction history of the Antalya slab in southern Anatolia. *Tectonics*, *37*(10), 3738–3759. https://doi.org/10.1029/2017TC004893

McPhee, P. J., & van Hinsbergen, D. J. J. (2019). Tectonic reconstruction of Cyprus reveals Late Miocene continental collision of Africa and Anatolia. *Gondwana Research*, *68*, 158–173. https://doi.org/10.1016/j.gr.2018.10.015

Meijers, M. J. M., Brocard, G. Y., Cosca, M. A., Lüdecke, T., Teyssier, C., Whitney, D. L., & Mulch, A. (2018). Rapid late Miocene surface uplift of the Central Anatolian Plateau margin. *Earth and Planetary Science Letters*, *497*, 29–41. https://doi.org/10.1016/j.epsl.2018.05.040

Menant, A., Sternai, P., Jolivet, L., Guillou-Frottier, L., & Gerya, T. (2016). 3D numerical modeling of mantle flow, crustal dynamics and magma genesis associated with slab roll-back and tearing: The eastern Mediterranean case. *Earth and Planetary Science Letters*, *442*, 93–107. https://doi.org/10.1016/j.epsl.2016.03.002

Molnar, P., England, P., & Martinod, J. (1993). Mantle dynamics, uplift of the Tibetan Plateau, and the Indian Monsoon. *Reviews of Geophysics*, *31*(4), 357. https://doi.org/10.1029/93RG02030

Niemann, J. D., Gasparini, N. M., Tucker, G. E., & Bras, R. L. (2001). A quantitative evaluation of Playfair's law and its use in testing long-term stream erosion models. *Earth Surface Processes and Landforms*, *26*(12), 1317–1332. https://doi.org/10.1002/esp.272

Öğretmen, N., Cipollari, P., Frezza, V., Faranda, C., Karanika, K., Gliozzi, E., et al (2018). Evidence for 1.5 km of uplift of the Central Anatolian Plateau's southern margin in the last 450 kyr and implications for its multiphased uplift history. *Tectonics*, *37*(1), 359–390. https://doi.org/10.1002/2017tc004805

Öğretmen, N., Frezza, V., Hudáčková, N., Gliozzi, E., Cipollari, P., Faranda, C., et al (2018). Early Pleistocene (Calabrian) marine bottom oxygenation and palaeoclimate at the southern margin of the Central Anatolian Plateau. *Italian Journal of Geosciences*, *137*(3), 425–464. https://doi.org/10.3301/ijg.2018.19

Okay, A. I., Zattin, M., & Cavazza, W. (2010). Apatite fission-track data for the Miocene Arabia-Eurasia collision. *Geology*, *38*(1), 35–38. https://doi.org/10.1130/G30234.1

Özbakır, A. D., Şengör, A. M. C., Wortel, M. J. R., & Govers, R. (2013). The Pliny-Strabo trench region: A large shear zone resulting from slab tearing. *Earth and Planetary Science Letters*, *375*, 188–195. https://doi.org/10.1016/j.epsl.2013.05.025

Perron, J. T., & Royden, L. (2013). An integral approach to bedrock river profile analysis: Integral approach to river profile analysis. *Earth Surface Processes and Landforms*, *38*(6), 570–576. https://doi.org/10.1002/esp.3302

Portner, D. E., Delph, J. R., Biryol, C. B., Beck, S. L., Zandt, G., Özacar, A. A., et al. (2018). Subduction termination through progressive slab deformation across Eastern Mediterranean subduction zones from updated P-wave tomography beneath Anatolia. *Geosphere*, *14*(3), 907–925. https://doi.org/10.1130/GES01617.1

Pritchard, D., Roberts, G. G., White, N. J., & Richardson, C. N. (2009). Uplift histories from river profiles. *Geophysical Research Letters*, *36*. https://doi.org/10.1029/2009GL040928

Quye-Sawyer, J., Whittaker, A. C., & Roberts, G. G. (2020). Calibrating fluvial erosion laws and quantifying river response to faulting in Sardinia, Italy. *Geomorphology*, *370*, 107388. https://doi.org/10.1016/j.geomorph.2020.107388

Racano, S., Jara-Muñoz, J., Cosentino, D., & Melnick, D. (2020). Variable quaternary uplift along the southern margin of the Central Anatolian Plateau inferred from modeling marine terrace sequences. *Tectonics*, *39*, e2019TC005921. https://doi.org/10.1029/2019tc005921

Radeff, G., Cosentino, D., Cipollari, P., Schildgen, T. F., Iadanza, A., Strecker, M., et al. (2016). Stratigraphic architecture of the upper Messinian deposits of the Adana Basin (Southern Turkey): Implications for the Messinian salinity crisis and the Taurus petroleum system. *Italian Journal of Geosciences*, *135*(3), 408–424. https://doi.org/10.3301/ijg.2015.18

Radeff, G., Schildgen, T. F., Cosentino, D., Strecker, M. R., Cipollari, P., Darbaş, G., & Gürbüz, K. (2017). Sedimentary evidence for late Messinian uplift of the SE margin of the Central Anatolian Plateau: Adana basin, southern Turkey. *Basin Research*, *29*, 488–514. https://doi.org/10.1111/bre.12159

Reilinger, R. E., McClusky, S. C., Oral, M. B., King, R. W., Toksoz, M. N., Barka, A. A., et al. (1997). Global positioning system measurements of present-day crustal movements in the Arabia-Africa-Eurasia plate collision zone. *Journal of Geophysical Research*, *102*(B5), 9983–9999. https://doi.org/10.1029/96JB03736

Roberts, G. G., Paul, J. D., White, N., & Winterbourne, J. (2012). Temporal and spatial evolution of dynamic support from river profiles: A framework for Madagascar: Dynamic support of Madagascar. *Geochemistry, Geophysics, Geosystems*, *13*. https://doi.org/10.1029/2012GC004040

Roberts, G. G., & White, N. (2010). Estimating uplift rate histories from river profiles using African examples. *Journal of Geophysical Research*, *115*. https://doi.org/10.1029/2009JB006692

Roberts, G. G., White, N. J., Martin-Brandis, G. L., & Crosby, A. G. (2012). An uplift history of the Colorado Plateau and its surroundings from inverse modeling of longitudinal river profiles. *Tectonics*, *31*. https://doi.org/10.1029/2012TC003107

Ruddiman, W. F., & Kutzbach, J. E. (1989). Forcing of late Cenozoic northern hemisphere climate by plateau uplift in southern Asia and the American west. *Journal of Geophysical Research*, *94*(D15), 18409. https://doi.org/10.1029/JD094iD15p18409

Salaün, G., Pedersen, H. A., Paul, A., Farra, V., Karabulut, H., Hatzfeld, D., et al. (2012). High-resolution surface wave tomography beneath the Aegean-Anatolia region: Constraints on upper-mantle structure: Tomography of Aegea-Anatolia upper mantle. *Geophysical Journal International*, *190*(1), 406–420. https://doi.org/10.1111/j.1365-246X.2012.05483.x

Scherler, D., & Schwanghart, W. (2020). Drainage divide networks—Part 2: Response to perturbations. *Earth Surface Dynamics*, *8*, 261–274. https://doi.org/10.5194/esurf-8-261-2020

Schildgen, T. F., Cosentino, D., Bookhagen, B., Niedermann, S., Yıldırım, C., Echtler, H., et al. (2012). Multi-phased uplift of the southern margin of the Central Anatolian plateau, Turkey: A record of tectonic and upper mantle processes. *Earth and Planetary Science Letters*, *317–318*, 85–95. https://doi.org/10.1016/j.epsl.2011.12.003

Schildgen, T. F., Cosentino, D., Caruso, A., Buchwaldt, R., Yıldırım, C., Bowring, S. A., et al. (2012). Surface expression of eastern Mediterranean slab dynamics: Neogene topographic and structural evolution of the southwest margin of the Central Anatolian Plateau, Turkey. *Tectonics*, *31*. https://doi.org/10.1029/2011TC003021

Schildgen, T. F., Yıldırım, C., Cosentino, D., & Strecker, M. R. (2014). Linking slab break-off, Hellenic trench retreat, and uplift of the Central and Eastern Anatolian plateaus. *Earth-Science Reviews*, *128*, 147–168. https://doi.org/10.1016/j.earscirev.2013.11.006

Schwanghart, W., & Scherler, D. (2014). Short communication: TopoToolbox 2—MATLAB-based software for topographic analysis and modeling in Earth surface sciences. *Earth Surface Dynamics*, *2*(1), 1–7. https://doi.org/10.5194/esurf-2-1-2014

Senel, M. (2002). *Geological map of Turkey—Konya*. General Directorate of Mineral Research and Exploration.

Şengör, A. M. C. (1980). *Türkiye'nin Neotektoniginin Esasları (Essentials of the Turkish Neotectonics)* (Vol. 2, pp. 40). Geological Society of Turkey.

Şengör, A. M. C., Gorür, N., & Şaroğlu, F. (1985). Strike-slip faulting and basin related formation in zones of tectonic escape: Turkey as a case study. In K. T. Biddle, & N. Christie-Blick (Eds.), *Strike-slip deformation, basin formation and sedimentation* (Vol. 37, pp. 227–440). Society of Economic Paleontologists and Mineralogists Special Publication.

Şengör, A. M. C., Özeren, M. S., Keskin, M., Sakınç, M., Özbakır, A. D., & Kayan, İ. (2008). Eastern Turkish high plateau as a small Turkic-type orogen: Implications for post-collisional crust-forming processes in Turkic-type orogens. *Earth-Science Reviews*, *90*(1), 1–48. https://doi.org/10.1016/j.earscirev.2008.05.002

Stearns, R. G. (1967). Warping of the Western Highland Rim Peneplain in Tennessee by ground-water sapping. *The Geological Society of America Bulletin*, *78*(9), 1111. https://doi.org/10.1130/0016-7606(1967)78[1111:WOTWHR]2.0.CO;2

Strecker, M. R., Alonso, R. N., Bookhagen, B., Carrapa, B., Hilley, G. E., Sobel, E. R., & Trauth, M. H. (2007). Tectonics and climate of the southern Central Andes. *Annual Review of Earth and Planetary Sciences*, *35*(1), 747–787. https://doi.org/10.1146/annurev.earth.35.031306.140158

Tarantola, A. (1988). Inverse problem theory. Methods for data fitting and model parameter estimation. *Geophysical Journal International*, *94*(1), 167–168. https://doi.org/10.1111/j.1365-246X.1988.tb03436.x

Tucker, G. E., & Slingerland, R. (1996). Predicting sediment flux from fold and thrust belts. *Basin Research*, *8*(3), 329–349. https://doi.org/10.1046/j.1365-2117.1996.00238.x

Tucker, G. E., & Whipple, K. X. (2002). Topographic outcomes predicted by stream erosion models: Sensitivity analysis and intermodel comparison. *Journal of Geophysical Research*, *107*, ETG1–ETG16. https://doi.org/10.1029/2001JB000162

Ulu, U. (2002). *Geological map of Turkey—Adana*. General Directorate of Mineral Research and Exploration.

Whipple, K. X., Forte, A. M., DiBiase, R. A., Gasparini, N. M., & Ouimet, W. B. (2017). Timescales of landscape response to divide migration and drainage capture: Implications for the role of divide mobility in landscape evolution. *Journal of Geophysical Research: Earth Surface*, *122*(1), 248–273. https://doi.org/10.1002/2016JF003973

Whipple, K. X., Kirby, E., & Brocklehurst, S. H. (1999). Geomorphic limits to climate-induced increases in topographic relief. *Nature*, *401*(6748), 39–43. https://doi.org/10.1038/43375

Whipple, K. X., & Tucker, G. E. (1999). Dynamics of the stream-power river incision model: Implications for height limits of mountain ranges, landscape response timescales, and research needs. *Journal of Geophysical Research*, *104*(B8), 17661–17674. https://doi.org/10.1029/1999JB900120

Wickert, A. D., & Schildgen, T. F. (2019). Long-profile evolution of transport-limited gravel-bed rivers. *Earth Surface Dynamics*, *7*, 17–43. https://doi.org/10.5194/esurf-7-17-2019

Wobus, C., Whipple, K. X., Kirby, E., Snyder, N., Johnson, J., Spyropolou, K., et al. (2006). Tectonics from topography: Procedures, promise, and pitfalls. In S. D. Willett, N. Hovius, M. T. Brandon, & D. M. Fisher (Eds.), *Special Paper 398: Tectonics, Climate, and Landscape Evolution* (Vol. 398, pp. 55–74). Geological Society of America. https://doi.org/10.1130/2006.2398(04)

Wortel, M. J. R., & Spakman, W. (2000). Subduction and slab detachment in the Mediterranean-Carpathian region. *Science*, *290*(5498), 1910–1917. https://doi.org/10.1126/science.290.5498.1910

Yildirim, C., Melnick, D., Ballato, P., Schildgen, T. F., Echtler, H., Erginal, A. E., et al. (2013). Differential uplift along the northern margin of the Central Anatolian Plateau: Inferences from marine terraces. *Quaternary Science Reviews*, *81*, 12–28. https://doi.org/10.1016/j.quascirev.2013.09.011

Yildirim, C., Schildgen, T. F., Echtler, H., Melnick, D., Bookhagen, B., Çiner, A., et al. (2013). Tectonic implications of fluvial incision and pediment deformation at the northern margin of the Central Anatolian Plateau based on multiple cosmogenic nuclides: Uplift rate in the Central Pontides. *Tectonics*, *32*(5), 1107–1120. https://doi.org/10.1002/tect.20066

York, D., Evensen, N. M., Martínez, M. L., & De Basabe Delgado, J. (2004). Unified equations for the slope, intercept, and standard errors of the best straight line. *American Journal of Physics*, *72*(3), 367–375. https://doi.org/10.1119/1.1632486

Zhisheng, A., Kutzbach, J. E., Prell, W. L., & Porter, S. C. (2001). Evolution of Asian monsoons and phased uplift of the Himalaya-Tibetan plateau since Late Miocene times. *Nature*, *411*(6833), 62–66. https://doi.org/10.1038/35075035

Reference From the Supporting Information

Jess, S., Koehn, D., Fox, M., Enkelmann, E., Sachau, T., & Aanyu, K. (2020). Paleogene initiation of the western branch of the East African Rift: The uplift history of the Rwenzori Mountains, western Uganda. *Earth and Planetary Science Letters*, *552*, 116593. https://doi.org/10.1016/j.epsl.2020.116593